Energetics of Barotropic and Baroclinic Tides in the Monterey Bay Area

Dujuan Kang * and Oliver Fringer

Department of Civil and Environmental Engineering, Stanford University, Stanford, California

* *Corresponding author address:* Dujuan Kang, Department of Civil and Environmental Engineering, Stanford University, Stanford, CA 94305.

E-mail: kangdj@stanford.edu

ABSTRACT

A detailed energy analysis of the barotropic and baroclinic M_2 tides in the Monterey Bay area is performed. We first derive a theoretical framework for analyzing internal tide energetics based on the complete form of the barotropic and baroclinic energy equations, which include the full nonlinear and nonhydrostatic energy flux contributions as well as an improved evaluation of the available potential energy. This approach is implemented in the hydrodynamic SUNTANS model. Results from three-dimensional, high-resolution SUNTANS simulations are analyzed to estimate the tidal energy partitioning among generation, radiation, and dissipation. A 200 km $\times$ 230 km domain including all typical topographic features in this region is used to represent the Monterey Bay area. Of the 152 MW energy lost from the barotropic tide, approximately 133 MW (88%) is converted into baroclinic energy through internal tide generation, and 42% (56 MW) of this baroclinic energy radiates away into the open ocean. The tidal energy partitioning depends greatly on the topographic features. The Davidson Seamount is most efficient at baroclinic energy generation and radiation, while the Monterey Submarine Canyon acts as an energy sink. Energy flux contributions from nonlinear and nonhydrostatic effects are also examined. In the Monterey Bay area, the nonlinear and nonhydrostatic contributions are quite small. Moreover, we investigate the character of internal tide generation and find that in the Monterey Bay area the generated baroclinic tides are mainly linear and in the form of internal tidal beams. Comparison of the modeled tidal conversion to previous theoretical estimates shows that they are consistent with one another.

1. Introduction

The ocean is a key component of the Earth's climate system, and mixing processes are critical in determining its distribution of salt, heat, and energy. The tides are one of the major sources of energy to mix the ocean. Studies have shown that 25-30% of the global barotropic tidal energy is lost in the deep ocean (Munk and Wunsch 1998; Egbert and Ray 2000, 2001). Internal tides are believed to play an important role in transferring this energy into deep ocean turbulence (Figure 1). When the barotropic tide flows over rough topographic features, a portion of the barotropic energy is lost directly through local dissipation and mixing, while the other portion is lost to the generation of internal (baroclinic) tides. This generated baroclinic energy either dissipates locally or radiates into the open ocean.

In the past few years significant effort has been made to estimate regional internal tide energetics using numerical simulations. Regions studied include the Northern British Columbia Coast (Cummins and Oey 1997), the Hawaiian Ridge (Merrifield et al. 2001; Merrifield and Holloway 2002; Carter et al. 2008), the East China Sea (Niwa and Hibiya 2004), the Monterey Bay region (Jachec et al. 2006; Carter 2010; Hall and Carter 2011), and the Mid-Atlantic Ridge (Zilberman et al. 2009). All of these studies employed the hydrostatic Princeton Ocean Model (POM) (Blumberg and Mellor 1987) except for the work by Jachec et al. (2006), which employed the nonhydrostatic SUNTANS model (Fringer et al. 2006). Some authors estimated the barotropic-to-baroclinic energy conversion using the hydrostatic portion of baroclinic energy flux divergence (Cummins and Oey 1997; Merrifield et al. 2001; Merrifield and Holloway 2002; Jachec et al. 2006), while others used the conversion term derived from barotropic and baroclinic energy equations (Niwa and Hibiya 2004; Carter et al.

2008).

Monterey Bay lies along the Central U. S. West Coast. It consists of the prominent Monterey Submarine Canyon (MSC), numerous ridges and smaller canyons to the north and south, and a continental slope and break region (Figure 2). This area is exposed to the large- and meso-scale variations of the California Current System as well as the tidal currents. The complex bathymetry is favorable for internal tide generation and energetic internal wave activity has been observed in the submarine canyon (Petruncio et al. 1998; Kunze et al. 2002; Carter and Gregg 2002). Jachec et al. (2006) performed simulations using the nonhydrostatic SUNTANS model to simulate internal tides in the Monterey Bay area. They determined that the Sur Platform region is the primary source for the M_2 internal tidal energy flux observed within MSC. The total baroclinic energy generated within their domain (outlined by black lines in Figure 2) is approximately 52 MW.

In this paper we extend the work of Jachec et al. (2006) and perform a detailed analysis of the energetics in the Monterey Bay area by understanding the relative contribution of different regions in the Bay to the overall energetics. We provide a theoretical framework for accurate evaluation of the tidal energy flux budget by including nonlinear and nonhydrostatic contributions. We conduct numerical simulations of internal tides in the Monterey Bay area and estimate the tidal energy budget based on the theoretical framework. A brief derivation of the barotropic and baroclinic energy equations is presented in Section 2. Subsequent sections focus on the numerical simulations which include the model setup and validation in Section 3, and the energetics analysis in Section 4. Section 5 examines the generation characteristics and compares the model estimate with previous theoretical results. Finally, conclusions are summarized in Section 6.

2. Theoretical framework

We derive the barotropic and baroclinic energy equations to study the energetics of barotropic and baroclinic tides. These equations provide a theoretical framework for the numerical evaluation of the tidal energy budget in subsequent sections. Here we provide a brief derivation of the equations. More detail is provided in Kang (2010) (available at http://purl.stanford.edu/sv691gk5449). The derivation is based on the governing equations in SUNTANS which simulates the three-dimensional Reynolds-averaged Navier-Stokes equations under the Boussinesq approximation, along with the density transport equation and the continuity equation,

$$\begin{aligned}
\frac{\partial \mathbf{u}}{\partial t} + \mathbf{u}\cdot\nabla\mathbf{u} &= -2\boldsymbol{\Omega}\times\mathbf{u} - \frac{1}{\rho_0}\nabla p - \frac{g}{\rho_0}\rho\mathbf{k} \\
&+ \nabla_H\cdot(\nu_H\nabla_H\mathbf{u}) + \frac{\partial}{\partial z}\left(\nu_V\frac{\partial \mathbf{u}}{\partial z}\right), \qquad (1)\\
\frac{\partial \rho}{\partial t} + \mathbf{u}\cdot\nabla\rho &= \nabla_H\cdot(\kappa_H\nabla_H\rho) + \frac{\partial}{\partial z}\left(\kappa_V\frac{\partial \rho}{\partial z}\right), \qquad (2)\\
\nabla\cdot\mathbf{u} &= 0, \qquad (3)
\end{aligned}$$

where $\mathbf{u} = (u, v, w)$ is the velocity vector and $\boldsymbol{\Omega}$ is the Earth's angular velocity vector. ν and κ, in units of $\mathrm{m}^2\ \mathrm{s}^{-1}$, are the eddy viscosity and eddy diffusivity, respectively. $(\ )_H$ and $(\ )_V$ are the horizontal and vertical components of a variable or operator. In SUNTANS, transport equations for temperature and salinity are solved individually, and a state equation is employed to compute density from temperature, salinity, and pressure (Millero et al. 1980; Millero and Poisson 1981). Here we only list the density transport equation (2) to make the derivation clearer. The total density is given by

$$\rho(x, y, z, t) = \rho_0 + \rho_b(z) + \rho'(x, y, z, t), \qquad (4)$$

where ρ_0 is the constant reference density, ρ_b is the background density, and ρ' is the perturbation density due to wave motions. The pressure is split into its hydrostatic (p_h) and nonhydrostatic (q) parts with $p = p_h + q$, where the hydrostatic pressure can be further decomposed with

$$\begin{aligned} p_h &= p_0 + p_b + p' \,, \\ &= \rho_0 g(\eta - z) + g\int_z^\eta \rho_b \, dz + g\int_z^\eta \rho' \, dz \,, \end{aligned} \tag{5}$$

where η is the free surface elevation. The reference pressure p_0 and the background pressure p_b include the part due to barotropic heaving by free surface movement since they are integrated to the free surface in our definition. In SUNTANS, the nonhydrostatic pressure, q is solved by employing the pressure correction method. In the computation, a three-dimensional Poisson equation for the nonhydrostatic pressure arises. This equation is the most computational demanding portion of a nonhydrostatic solver (Fringer et al. 2006).

To obtain the barotropic and baroclinic equations, we first split the velocity into its barotropic and baroclinic parts as $\mathbf{u} = \mathbf{U} + \mathbf{u}'$. The barotropic velocities are defined as

$$\mathbf{U}_H = \frac{1}{H}\int_{-d}^{\eta} \mathbf{u}_H \, dz = \frac{1}{H}\overline{\mathbf{u}_H} \,, \tag{6}$$

$$W = -\nabla_H \cdot [(d+z)\mathbf{U}_H] \,, \tag{7}$$

where $\overline{(\cdot)} = \int_{-d}^{\eta}(\cdot)\, dz$ is the depth-integration of a quantity from the bottom $z = -d(x,y)$ to the surface $z = \eta(x,y,t)$, and the total water depth is $H = \eta + d$. Based on the velocity decomposition, the kinetic energy density, in units of J m^{-3}, is decomposed as

$E_k = E_{k0} + E'_k + E'_{k0}$, where

$$E_{k0} = \frac{1}{2}\rho_0 \left(U^2 + V^2\right) , \tag{8}$$

$$E'_k = \frac{1}{2}\rho_0 \left(u'^2 + v'^2 + w^2\right) , \tag{9}$$

$$E'_{k0} = \rho_0 \left(Uu' + Vv'\right) . \tag{10}$$

Here E_{k0} is the barotropic horizontal kinetic energy density, E'_k is the baroclinic kinetic energy density, and E'_{k0} is the cross term which vanishes upon depth-integration. Following Gill (1982), the perturbation potential energy due to surface elevation, in units of J m^{-2}, is given by

$$\overline{E_{p0}} = \frac{1}{2}\rho_0 g \eta^2 . \tag{11}$$

The available potential energy density, in units of J m^{-3}, is defined as

$$E'_p = \int_{z-\zeta}^{z} g \left[\rho_b(z) + \rho'(z) - \rho_b(z')\right] dz' , \tag{12}$$

where ζ is the vertical displacement of a fluid particle due to wave motions. Kang and Fringer (2010) provided a clear graphical interpretation of this and two other APE definitions (Figure 1 in their paper). This definition is an exact expression of the local APE because it computes the true active potential energy between the perturbed and unperturbed density profiles. It has been employed in analyzing internal wave energetics by numerous authors (Scotti et al. 2006; Lamb 2007; Lamb and Nguyen 2009; Kang and Fringer 2010).

Applying the variable decompositions and the boundary conditions, we obtain the depth-integrated barotropic and baroclinic energy equations as

$$\frac{\partial}{\partial t}\left(\overline{E_{k0}} + \overline{E_{p0}}\right) + \nabla_H \cdot \overline{\mathbf{F}_0} = -\overline{C} - \overline{\epsilon_0} - D_0 , \tag{13}$$

$$\frac{\partial}{\partial t}\left(\overline{E'_k} + \overline{E'_p}\right) + \nabla_H \cdot \overline{\mathbf{F}'} = \overline{C} - \overline{\epsilon'} - D' , \tag{14}$$

where the depth-integrated barotropic and baroclinic energy flux terms, with the small unclosed terms neglected (see Kang (2010)), are given by

$$\overline{\mathbf{F}_0} = \underbrace{\mathbf{U}_H\overline{E_{k0}}}_{\text{Advection}} \underbrace{+\mathbf{U}_H H\rho_0 g\eta + \mathbf{U}_H\overline{p'} + \mathbf{U}_H\overline{q}}_{\text{Pressure work}} \underbrace{-\overline{\nu_H\nabla_H E_{k0}}}_{\text{Diffusion}}, \tag{15}$$

$$\overline{\mathbf{F}'} = \underbrace{\overline{\mathbf{u}_H E'_k} + \overline{\mathbf{u}_H E'_{k0}} + \overline{\mathbf{u}_H E'_p}}_{\text{Advection}} \underbrace{+\overline{\mathbf{u}'_H p'} + \overline{\mathbf{u}'_H q}}_{\text{Pressure work}} \underbrace{-\overline{\nu_H\nabla_H E'_k} - \overline{\kappa_H\nabla_H E'_p}}_{\text{Diffusion}}, \tag{16}$$

where the contributions from energy advection, pressure work, and diffusion have been labeled. The barotropic-to-baroclinic conversion rate, the dissipation rates and the bottom drag terms are given by

$$\overline{C} = \overline{\rho' g W} - \overline{\frac{\partial q}{\partial z} W}\,, \tag{17}$$

$$\epsilon_0 = \rho_0\nu_H\nabla_H\mathbf{U}_H\cdot\nabla_H\mathbf{U}_H\,, \tag{18}$$

$$\epsilon' = \epsilon'_k + \epsilon'_p\,, \tag{19}$$

$$\begin{aligned}\epsilon'_k &= \rho_0\nu_H\nabla_H\mathbf{u}'_H\cdot\nabla_H\mathbf{u}'_H + \rho_0\nu_V\frac{\partial\mathbf{u}'_H}{\partial z}\cdot\frac{\partial\mathbf{u}'_H}{\partial z}\\ &+ \rho_0\nu_H\nabla_H w\cdot\nabla_H w + \rho_0\nu_V\frac{\partial w}{\partial z}\frac{\partial w}{\partial z}\,,\end{aligned} \tag{20}$$

$$\epsilon'_p = g\kappa_H\nabla_H\rho'\cdot\nabla_H\zeta + g\kappa_V\frac{\partial(\rho_b+\rho')}{\partial z}\frac{\partial\zeta}{\partial z}\,, \tag{21}$$

$$D_0 = \rho_0 C_d\left|\mathbf{u}_H\right|(uU+vV)\,, \qquad \text{at } z=-d \tag{22}$$

$$D' = \rho_0 C_d\left|\mathbf{u}_H\right|\left(uu'+vv'+w^2\right)\,, \quad \text{at } z=-d \tag{23}$$

where C_d is the bottom drag coefficient.

The time-averaged forms of equations (13) and (14) are given by

$$\frac{1}{T}\Delta\overline{E_0} + \nabla_H\cdot\left\langle\overline{\mathbf{F}_0}\right\rangle = -\left\langle\overline{C}\right\rangle - \left\langle\overline{\epsilon_0}+D_0\right\rangle\,, \tag{24}$$

$$\frac{1}{T}\Delta\overline{E'} + \nabla_H\cdot\left\langle\overline{\mathbf{F}'}\right\rangle = \left\langle\overline{C}\right\rangle - \left\langle\overline{\epsilon'}+D'\right\rangle\,, \tag{25}$$

where $\langle\cdot\rangle = \frac{1}{T}\int_t^{t+T}(\cdot)\,d\tau$ is the time-average of a quantity over a time interval T. Therefore, net changes of the depth-integrated barotropic and baroclinic total energy are given by

$$\Delta\overline{E_0} = \left(\overline{E_{k0}} + \overline{E_{p0}}\right)\Big|_{t+T} - \left(\overline{E_{k0}} + \overline{E_{p0}}\right)\Big|_t , \tag{26}$$

$$\Delta\overline{E'} = \left(\overline{E'_k} + \overline{E'_p}\right)\Big|_{t+T} - \left(\overline{E'_k} + \overline{E'_p}\right)\Big|_t . \tag{27}$$

For a periodic system with period T, $\Delta\overline{E_0}$ and $\Delta\overline{E'}$ tend to zero and thus the first term in equations (24)-(25) vanishes. The remaining terms describe the energy balance associated with tidal dissipation processes. The $\nabla_H \cdot \left\langle\overline{\mathbf{F}_0}\right\rangle$ term represents the total barotropic energy that is available for conversion to baroclinic energy, $\left\langle\overline{C}\right\rangle$ represents the portion of the barotropic energy that is converted into baroclinic energy, and the $\nabla_H \cdot \left\langle\overline{\mathbf{F}'}\right\rangle$ term represents the portion of the converted baroclinic energy that radiates from the conversion site. Local dissipation occurs along with the conversion and radiation processes, and they are measured by the barotopic ($-\left\langle\overline{\epsilon_0} + D_0\right\rangle$) and baroclinic ($-\left\langle\overline{\epsilon'} + D'\right\rangle$) dissipation terms, respectively. Figure 1 illustrates the tidal energy budget using these terms.

This approach presents an exact measure of the barotopic-to-baroclinic tidal energy conversion and highlights its relation to the total convertible barotropic energy and the radiated baroclinic energy. The conversion term includes two parts representing the hydrostatic $\overline{\rho' g W}$ and nonhydrostatic $-\overline{\frac{\partial q}{\partial z} W}$ contributions, respectively. Furthermore, we consider the contributions to the energy flux budget from the available potential energy flux and the kinetic energy fluxes due to nonlinear and nonhydrostatic effects. In many previous studies, only the dominant hydrostatic baroclinic energy term, $\nabla_H \cdot (\overline{\mathbf{u}' p'})$, was calculated to represent the conversion (Cummins and Oey 1997; Merrifield et al. 2001; Merrifield and Holloway 2002; Jachec et al. 2006). Niwa and Hibiya (2004) evaluated the conversion using a similar term as

$\overline{\rho' g W}$, which is the hydrostatic part of our conversion term (17). Carter et al. (2008) derived barotropic and baroclinic equations from POM's hydrostatic governing equations and thus did not include the nonhydrostatic contribution. Their approach distinguishes between the conversion from the barotropic input and the baroclinic radiation. However, they used a linear APE definition, which may cause error in the presence of strongly nonlinear stratification (Kang and Fringer 2010). MacCready et al. (2009) provided the kinetic and potential energy equations for the hydrostatic Regional Ocean Modeling System (ROMS) (Haidvogel et al. 2000). They did not derive the barotropic and baroclinic energy equations individually and thus were unable to estimate the barotropic-to-baroclinic tidal conversion. However, they split the hydrostatic pressure into barotropic and baroclinic parts and therefore were able to evaluate the corresponding tidal energy flux budget. Moreover, their approach can estimate the contribution of the winds to the total energy budget because a wind stress term was included in their energy equations.

3. Numerical simulations

a. Model setup

We employ the SUNTANS model of Fringer et al. (2006) with modifications by Zhang et al. (2011) to incorporate high-resolution scalar advection. The simulation domain extends approximately 200 km north and south of Moss Landing, and 400 km offshore (Figure 2). The domain of Jachec et al. (2006) ($\sim$200 km alongshore $\times$ 90 km offshore) is outlined by black lines in Figure 2. Compared to their domain, ours is larger and allows the evolution of

offshore-propagating waves. The horizontal unstructured grid for our simulations is depicted in Figure 3. The grid resolution smoothly transitions from roughly 80 m within the Bay to 11 km along the offshore boundary. Approximately 60% of the grid cells have a resolution smaller than 1000 m, and 80% of the grid cells have a resolution smaller than 1600 m. In the vertical, there are 120 z-levels with thickness stretching from roughly 6.6 m at the surface to 124 m in the deepest location, which provides better vertical resolution in the shallow regions. The vertical locations of grid centers are indicated by the black dots in Figure 4. In total, the mesh consists of approximately 6 million grid cells in 3D.

The initial free-surface and velocity field are initialized as quiescent throughout the domain. As shown in Figure 4, the initial stratification is specified with horizontally-homogeneous temperature and salinity profiles obtained from the 2006 AESOP (Assessing the Effectiveness of Submesoscale Ocean Parameterizations) field experiment (Terker et al. 2011). We use linear extrapolation to extend the observed profiles from 2000 m to 4800 m.

At the coastline, we apply the no-flow condition, while at the three open boundaries the barotropic velocities are specified as

$$\mathbf{U}_b = \mathbf{U}_0 \cos\left(\omega t + \phi\right) \ , \tag{28}$$

where ω is the M_2 tidal frequency, and the corresponding amplitude $\mathbf{U}_0$ and phase ϕ are obtained with the OTIS global tidal model (Egbert and Erofeeva 2002). Rather than employ a partially-clamped condition (Blayo and Debreu 2005), we found that a clamped condition was suitable because the transient barotropic wave decays after two tidal cycles and little barotropic energy reflects off of the boundaries during the simulations. In order to prevent transient oscillations associated with impulsively starting the tidal forcing, the boundary

velocities are spun up over a time scale of τ_r to approach the imposed forcing with

$$\mathbf{U}_{b_{actual}} = \mathbf{U}_b \left[1 - \exp\left(-\frac{t}{\tau_r}\right)\right] , \tag{29}$$

where τ_r is set to one day in the simulations. Furthermore, at all three open boundaries a sponge layer is imposed to absorb the internal waves and minimize the reflection of baroclinic energy into the domain. Following Zhang (2010), the sponge layer is applied as a damping term on the right-hand side of the horizontal momentum equation of the form

$$\mathbf{S}_H = -\frac{\mathbf{u}'_H}{\tau_s} \exp\left(-\frac{4r}{L_s}\right) , \tag{30}$$

where r is the distance to the closest open boundary and L_s is the width of the sponge layer. The damping time scale τ_s is determined with

$$\tau_s = -\frac{L_s}{4c \log(1-\alpha)} , \tag{31}$$

where c is the internal wave speed and α is the decay rate. The first mode M_2 internal wave speed in a depth of 3000 m is $c_1 = 1.98$ ms^{-1} and the corresponding wave length is approximately 88 km. In our simulations this value is used as the width of the sponge layer, which absorbs $\alpha = 99.99\%$ of the first mode baroclinic wave energy over a time scale of τ_s =2750 s.

The simulation begins on August 18th, 2006 (year day 229) and is run for 18 M_2 tidal cycles. A time step size of $\Delta t = 18$ s is used to ensure stability. In the simulation no turbulence model is employed. Diffusion of scalars is ignored by setting $\kappa_H = \kappa_V = 0$. A horizontal eddy-viscosity of $\nu_H = 1$ m^{2}s^{-1} and a vertical viscosity of $\nu_V = 5 \times 10^{-3}$ m^{2}s^{-1} are applied uniformly throughout the domain. In a sensitivity test we found that the energetics are weakly affected by changing the viscosities by one order of magnitude (see Appendix).

A constant bottom drag coefficient of $C_D = 0.0025$ and a constant Coriolis frequency of $f = 8.7 \times 10^{-5}$ rad s^{-1} are specified. For the 18-M_2-cycle simulation, the model runs in 1.25 wall-clock days, or 3830 CPU hours using 128 processors on the MJM Linux Networx Intel Xeon EM64T Cluster at the Army Research Laboratory DoD Supercomputing Resource Center (ARL DSRC).

b. Model validation

In previous numerical studies of internal tides in Monterey Bay, SUNTANS has shown a high level of skill in predicting the water surface and velocities in the canyon (Jachec et al. 2006; Jachec 2007). Here we do two more comparisons.

First, the sea-surface predictions are compared with the observations at two water-level gauges (Monterey and Point Reyes) maintained by the National Oceanic and Atmospheric Administration (NOAA). The water level data at these two gauges cover our simulation period (available at http://tidesandcurrents.noaa.gov/). We employ the T-Tide package (Pawlowicz et al. 2002) to estimate the M_2 surface amplitudes and phases. For the observations, 6-minute NOAA data for August 15-29, 2006 are used for the harmonic analysis, while for the predictions, 6-minute model outputs of the last 10 M_2 cycles are used. To quantitatively evaluate the M_2 surface discrepancy between observations and model predictions, we compute the RMS error

$$E = \sqrt{\frac{1}{2}\left(A_o^2 + A_m^2\right) - A_o A_m \cos(G_o - G_m)}\,, \tag{32}$$

and the relative RMS error

$$R_E = \frac{E}{A_o}\,, \tag{33}$$

following previous studies (Cummins and Oey 1997; Carter et al. 2008; Carter 2010). Here subscripts o and m denote observed and model predicted amplitudes (A) and phases (G). For this case, the absolute and relative RMS errors are 0.37 cm and 0.8% at Monterey, while they are 2.1 cm and 3.9% at Point Reyes.

The model predictions are further compared with the field observations at an R/V FLIP station (hereinafter referred to as Station K) during the 2006 AESOP field experiment. The field data was provided by Dr. Jody Klymak and Dr. Robert Pinkel. Station K is located north of the Sur Platform as indicated in Figure 2. We examine the model performance in predicting the baroclinic features. Figure 5 compares the M_2 baroclinic (total minus depth-averaged) velocity profiles between observations and model predictions at Station K. An M_2 band-pass filter is applied to the original observations to obtain the M_2-fit baroclinic velocity profiles (Figure 5(a)). We implement the M_2 band-pass filtering in this way: the observed time series is first mapped to the frequency space via Fourier transform, then the amplitude of all frequencies are reduced to zero except for the band within 5% of M_2, and finally an inverse Fourier transform is employed to obtain the M_2-fit time series. Intermittent behaviour can be detected in the observed baroclinic velocities. The intermittency of the internal tide has been attributed to the variability in background conditions (Manders et al. 2004; Kurapov et al. 2010). Station K is under the influence of wind-driven upwelling, which may cause variable background stratification and hence result in the observed tidal intermittency. The modeled baroclinic velocities do not show intermittent behaviour because the large- and meso-scale wind-driven features are not considered in this simulation. Due to intermittency, spectral analysis can underestimate the tidal velocity magnitudes (Kurapov et al. 2010). This may explain why the strength of the M_2-fit baroclinic velocities (Figure 5(a)) are

slightly weaker than the model predictions (Figure 5(b)). The model predictions capture the vertical structure of the baroclinic velocities. The multi-mode feature can be seen in both field observations and model predictions, which indicates the existence of higher-mode baroclinic tides at this location. We finally compute the relative RMS errors to quantitatively assess the differences between observed and modeled M_2 baroclinic velocities. The average relative RMS errors for u' and v' are 69.4% and 34.6%, respectively.

4. Energetics

We evaluate the depth-integrated, time-averaged barotropic and baroclinic energy equations (24) and (25) for the energy analysis in this section. They are averaged over the last six M_2 tidal cycles of the 18-M_2-cycle simulation. Because the system is periodic, the first term in equation (24)-(25) tends to zero upon period-averaging. We therefore obtain the balance relations

$$\nabla_H \cdot \left\langle \overline{\mathbf{F}_0} \right\rangle = -\left\langle \overline{C} \right\rangle - \left\langle \overline{\epsilon_0} + D_0 \right\rangle , \tag{34}$$

$$\nabla_H \cdot \left\langle \overline{\mathbf{F}'} \right\rangle = \left\langle \overline{C} \right\rangle - \left\langle \overline{\epsilon'} + D' \right\rangle . \tag{35}$$

The model computes all the energy terms in the barotropic and baroclinic equations. In the following analysis, the conversion rate, $\left\langle \overline{C} \right\rangle$, and the energy flux divergence terms, $\nabla_H \cdot \left\langle \overline{\mathbf{F}_0} \right\rangle$ and $\nabla_H \cdot \left\langle \overline{\mathbf{F}'} \right\rangle$, are from direct model outputs. However, the barotropic and baroclinic dissipation rates are inferred from the above balance relations as in Niwa and Hibiya (2004). Carter et al. (2008) analyzed the domain-integrated energy budget in the same way. A set of sensitivity tests have shown that the conversion, divergence, and inferred dissipation

terms are nearly independent of the dissipation parameters (ν_H, ν_V and C_d), while the directly computed dissipation depends greatly on the dissipation parameters (See Appendix for details). In the simulations, the values of the diffusion parameters are not the realistic ocean values but instead are based on the stability requirements of numerical differencing. Moreover, in the real ocean the eddy viscosities and bottom drag are functions of location and time, while in the simulations we only apply constant values throughout the domain. Therefore, even though we are able to compute the dissipation directly, it may not truly represent the physical dissipation in the real ocean. For this reason, the inferred dissipation, which is nearly independent of the dissipation parameters, is used for the energy analysis in this section. Please note that this inferred dissipation includes both the physical portion and the numerical portion, as described in the Appendix.

a. Horizontal structure

Figure 6 illustrates the horizontal distribution of the depth-integrated baroclinic energy flux vectors, $\left\langle \overline{\mathbf{F}'} \right\rangle$. Large fluxes are seen in the vicinity of four topographical features, which include a northern shelf-slope region (b), the MSC (c), the Sur Ridge-Platform region (d), and the Davidson Seamount (e). The energy budget within each subdomain is discussed in the next section. Figure 7 shows the horizontal distribution of the depth-integrated barotropic-to-baroclinic conversion rate, $\langle \overline{C} \rangle$. Red color represents positive energy conversion rate, which implies generation of internal tides, and the figure shows that most of the generation is contained within the 200-m and 3000-m isobaths. Negative energy conversion rate (blue color) represents energy transfer from the baroclinic tide to the barotropic tide. This is due to

the phase difference between locally- and remotely-generated baroclinic tides, and therefore indicates multiple generation sites (Zilberman et al. 2009). Significant negative conversion occurs within the MSC because the locally generated baroclinic tides interact with those generated at the North Sur Platform region. Large baroclinic energy can be seen radiating from North Sur Platform into the MSC following the canyon bathymetry (Figure 6). This effect was also demonstrated by Jachec et al. (2006), Carter (2010), and Hall and Carter (2011). Figure 8 illustrates the divergence of the depth-integrated baroclinic energy flux, $\nabla_H \cdot \left\langle \overline{\mathbf{F}'} \right\rangle$. The difference between Figure 7 and Figure 8, which represents the baroclinic dissipation rate, $\nabla_H \cdot \left\langle \overline{\mathbf{F}'} \right\rangle - \left\langle \overline{C} \right\rangle$, is shown in Figure 9. Large baroclinic energy dissipation occurs near the locations of strong internal tide generation.

b. Energy flux budget

The total power within a region is obtained by area-integrating the period-averaged and depth-integrated energy terms to give

$$\text{BT Input} = -\sum \nabla_H \cdot \left\langle \overline{\mathbf{F}_0} \right\rangle \, \Delta A \,, \tag{36}$$

$$\text{Conversion} = \sum \left\langle \overline{C} \right\rangle \, \Delta A \,, \tag{37}$$

$$\text{BC Radiation} = \sum \nabla_H \cdot \left\langle \overline{\mathbf{F}'} \right\rangle \, \Delta A \,, \tag{38}$$

$$\text{BT Dissipation} = \sum \left(\nabla_H \cdot \left\langle \overline{\mathbf{F}_0} \right\rangle + \left\langle \overline{C} \right\rangle \right) \, \Delta A \,, \tag{39}$$

$$\text{BC Dissipation} = \sum \left(\nabla_H \cdot \left\langle \overline{\mathbf{F}'} \right\rangle - \left\langle \overline{C} \right\rangle \right) \, \Delta A \,, \tag{40}$$

$$\text{Total Dissipation} = \sum \left(\nabla_H \cdot \left\langle \overline{\mathbf{F}_0} \right\rangle + \nabla_H \cdot \left\langle \overline{\mathbf{F}'} \right\rangle \right) \, \Delta A \,, \tag{41}$$

where $\sum$ implies summation of the grid cells within a particular region and ΔA is the area of each grid cell. We first study the energy distribution as a function of bottom depth. Each term in equations (36)-(41) is summed over cells bounded by isobaths at increments of 200 m. The lower panel in Figure 10 compares the energy distribution in 200-m isobath bounded bins, while the upper panel compares the cumulative sum. In the region shallower than 200 m, only a small portion of the input barotropic energy is converted into baroclinic energy, and the negative baroclinic energy radiation implies that baroclinic energy generated in deeper regions flows into this shallow region and is then dissipated. In the region deeper than 2200 m, nearly all of the input barotropic energy is converted to baroclinic energy. The radiated baroclinic energy is large in the region between the 1400-m and 2600-m isobaths, and is much smaller in other regions. Most of the barotropic energy dissipation occurs in the region shallower than 2000 m, while the baroclinic energy dissipation occurs at all depths with two peaks near 1200 m and within 200 m. Figure 11 illustrates a schematic of the energy budget for the shelf and slope regions bounded by the 200-m and 3000-m isobaths. Barotropic energy is lost at a rate of 147 MW to the slope region and approximately 87% of this energy is converted into baroclinic energy. Most of this generated baroclinic energy is dissipated locally, while the remaining portion (38%) is radiated. The shelf region acts as a baroclinic energy sink because it dissipates both the energy generated locally and the portion flowing into it from the slope region.

We list the detailed M_2 energy budget (Table 1) for the five subdomains (a)-(e) indicated in Figure 6. Subdomain (a), a 200 km $\times$ 230 km domain, is used to represent the Monterey Bay area because it includes all typical topographic features in this area. For this area, approximately 133 MW (88%) of the 152 MW barotropic energy is converted into baroclinic

energy, and 56 MW (42%) of this generated baroclinic energy radiates away. The baroclinic dissipation (77 MW) is roughly four times as large as the barotropic dissipation (19 MW). The tidal energy budget depends strongly on topographic features as shown in Table 1. The Davidson Seamount and the Northern shelf-break region are the most efficient topographic features to convert ($\sim 94\%$) barotropic energy into baroclinic energy and then let it radiate out into the open ocean ($> 70\%$). The Sur Platform region also converts a large portion (87.5%) and radiates about half of the barotropic energy as baroclinic energy. The MSC acts as an energy sink because it does not radiate energy but instead absorbs the baroclinic energy from the Sur Platform region (Figure 6). In particular, the energy budget for the Davidson Seamount (subdomain (e)) is quite similar to that for the Hawaiian Islands by Carter et al. (2008), which shows that 85% of the barotropic energy that is converted into baroclinic energy, and 74% of this baroclinic energy radiates into the open ocean.

c. Energy flux contributions

As discussed in Section 2, our method computes the full energy fluxes and thus allows us to compare the contributions of different components. Here we choose subdomain (a) as our study domain. The baroclinic energy radiation within this region is computed by equation (38) as $\sum_{(a)} \left(\nabla_H \cdot \left\langle \overline{\mathbf{F}'} \right\rangle \right) \Delta A$. Based on equation (16), this baroclinic energy radiation has five contributions from kinetic energy advection ($\sum_{(a)} \left(\nabla_H \cdot \left\langle \overline{\mathbf{u}_H E'_k} + \overline{\mathbf{u}_H E'_{k0}} \right\rangle \right) \Delta A$), available potential energy advection ($\sum_{(a)} \left(\nabla_H \cdot \left\langle \overline{\mathbf{u}_H E'_p} \right\rangle \right) \Delta A$), hydrostatic pressure work ($\sum_{(a)} \left(\nabla_H \cdot \left\langle \overline{\mathbf{u}'_H p'} \right\rangle \right) \Delta A$), nonhydrostatic pressure work ($\sum_{(a)} \left(\nabla_H \cdot \left\langle \overline{\mathbf{u}'_H q} \right\rangle \right) \Delta A$), and energy diffusion ($\sum_{(a)} \left(\nabla_H \cdot \left\langle -\overline{\nu_H \nabla_H E'_k} - \overline{\kappa_H \nabla_H E'_p} \right\rangle \right) \Delta A$). Table 2 compares these five con-

tributions to the total baroclinic energy radiation in subdomain (a). The component due to hydrostatic pressure work (the traditional energy flux) is the dominant term. If we consider the total energy radiation as 100%, the hydrostatic contribution is $\sim$ 101% while the other terms account for the remaining -1%. The small advection and nonhydrostatic contributions imply that the internal tides in the Monterey Bay area are mainly linear and hydrostatic.

Vitousek and Fringer (2011) show that the horizontal grid spacing must be smaller than roughly half of the water depth to begin to resolve nonhydrostatic effects. Therefore, although the contribution of the nonhydrostatic pressure in our smulations is small and may be on the same order as errors in evaluating the overall tidally-averaged energy balance, the resolution we employ is sufficient to assess the role the nonhydrostatic pressure may play in the energetics. Figure 12 shows that the hydrostatic and nonhydrostatic energy fluxes oppose one another within MSC. This occurs because the effect of the nonhydrostatic pressure is to restrict the acceleration owing to the impact of vertical inertia. Hydrostatic models therefore tend to overpredict the energy flux particularly for strongly nonhydrostatic flows.

5. Generation characteristics

a. Parameter Space

Four nondimensional parameters are generally employed to discuss the character of internal tide generation, which is governed by the dimensional parameters listed in Table 3. The first parameter is the steepness parameter defined by

$$\epsilon_1 = \frac{\gamma}{s}\,, \tag{42}$$

where the topographic slope is given by

$$\gamma = \sqrt{\left(\frac{\partial h}{\partial x}\right)^2 + \left(\frac{\partial h}{\partial y}\right)^2}, \tag{43}$$

and the internal wave characteristic slope is given by

$$s = \frac{k}{m} = \sqrt{\frac{\omega^2 - f^2}{N^2 - \omega^2}}\,. \tag{44}$$

The steepness parameter is used to distinguish between subcritical ($\epsilon_1 < 1$) and supercritical topography ($\epsilon_1 > 1$). The topography is referred to as critical when $\epsilon_1 = 1$. Many studies have been carried out to understand the barotropic-to-baroclinic conversion over subcritical (Bell 1975; Llewellyn Smith and Young 2002; Balmforth et al. 2002) and supercritical topography (Khatiwala 2003; St. Laurent et al. 2003; Balmforth and Peacock 2009).

The second nondimensional parameter is the tidal excursion parameter defined by

$$\epsilon_2 = \frac{U_0 k_b}{\omega}\,, \tag{45}$$

which measures the ratio of the tidal excursion U_0/ω to the horizontal scale of the topography k_b^{-1}. Here U_0 is simply the maximum magnitude of the local barotropic flow. A better way night be to include the angle of the principle axis of the barotropic tidal ellipse with respect to the topography, but this produces results that were too noisy and therefore we just keep U_0. In general the excursion parameter is computed for a single ridge or shelf slope. However, since the local topographic scale is not generally known, we estimated it with $k_b = \gamma/h_0$ following Garrett and Kunze (2007), where $h_0 = H_0 - d$ is the topographic amplitude. In this study, the reference depth H_0 is defined by the maximum water depth in the studied domain. The excursion parameter is used to examine the nonlinearity of the waves (Balmforth et al. 2002; St. Laurent and Garrett 2002; Vlasenko et al. 2005; Legg and Huijts 2006; Garrett

and Kunze 2007). When $\epsilon_2 \ll 1$, linear internal tides are generated mainly at the forcing frequency ω. Over subcritical topography ($\epsilon_1 < 1$) most of the energy generation is in the first mode internal tide, while over critical or supercritical topography ($\epsilon_1 \geq 1$), higher modes are generated and their superposition creates internal tidal beams. At intermediate excursion ($\epsilon_2 \sim 1$), nonlinearity becomes important, and nonlinear internal wave bores, weak unsteady lee waves, and solitary internal waves may be generated depending on the topographic features. It has been found in numerical models that lee waves are also generated for $\epsilon_2 < 1$ over tall and steep topography (Legg and Huijts 2006; Legg and Klymak 2008; Buijsman et al. 2010). When $\epsilon_2 > 1$, in addition to bores and solitary internal waves, strong unsteady lee waves may form (Vlasenko et al. 2005).

The third nondimensional parameter is the ratio of topographic amplitude to the total water depth, which is given by

$$\delta = \frac{h_0}{H}\,. \tag{46}$$

This parameter has been used to investigate the role of finite ocean depth on internal wave generation (Llewellyn Smith and Young 2002; Khatiwala 2003; St. Laurent et al. 2003).

The last nondimensional parameter is the Froude number defined by

$$Fr = \frac{U_0}{Nh_0}\,, \tag{47}$$

which has been used to examine the obstruction of the flow by the topography (Legg and Huijts 2006; Legg and Klymak 2008). The Froude number and the first two nondimentional parameters are related to one another via

$$\frac{\epsilon_2}{\epsilon_1} = Fr\frac{kN}{m\omega}\,. \tag{48}$$

Based on (44), in the mid-frequency case ($f \ll \omega \ll N$) or the nonrotating and hydrostatic case ($f = 0$ & $k \ll m$), we have $k/m = \omega/N$ and hence $\epsilon_2/\epsilon_1 = Fr$. This relation was demonstrated in the parameter space diagram of Garrett and Kunze (2007) .

b. Energy distribution vs. parameters

Although internal wave generation is a complex process, we can summarize the behavior of the internal wave generation in Monterey Bay by plotting histograms of the conversion and divergence terms as functions of the criticality and excursion parameters. Here we compute the two parameters throughout subdomain (a). Figures 13(a) and (b) demonstrate the distribution of conversion and BC radiation as a function of the nondimensional parameters ϵ_1 and ϵ_2. The energy terms (37)-(38) as functions of the parameters are computed as the total sum of the energy within 20 bins. As seen in Figure 13, barotropic-to-baroclinic conversion (green bins) occurs predominantly in regions within which $\epsilon_1 = \gamma/s < 5$ and $\epsilon_2 = U_0 k_b/\omega < 0.06$. Under these conditions, baroclinic tides generated in this region are mainly linear and in the form of internal tidal beams (St. Laurent and Garrett 2002; Vlasenko et al. 2005; Garrett and Kunze 2007).

As expected, conversion of barotropic energy into baroclinic energy peaks for critical topography near $\epsilon_1 \sim 1$ as shown in Figure 13(a). More interesting, however, is that there is also a peak in conversion for a particular value of $\epsilon_2 \sim 0.005$, as shown in Figure 13(b). A peak in the conversion for a particular value of ϵ_2 implies that narrow ridges relative to the tidal excursion (i.e. large ϵ_2) do not efficiently convert barotropic energy, and wide ridges are weak converters as well. This may arise because the dissipative effects that are not included

in the parameter space strongly impact the generation physics for small and large values of ϵ_2 but play a minimal role for the optimal excursion parameter. One possible explanation is that narrow topography with respect to the tidal excursion (large ϵ_2) is relatively rough and so dissipates too much energy and is a poor converter of barotropic energy. The same may be true for relatively wide topography (small ϵ_2) in that dissipative mechanisms dominate when the topography over which the internal wave action occurs is extensive even if the associated currents are weak. This behavior was observed by Venayagamoorthy and Fringer (2007) in idealized simulations of internal waves interacting with slopes. They showed that there was an excursion parameter that optimized on-slope internal wave energy propagation. Too small an excursion parameter led to extensive bottom friction relative to the weak internal waves, while too large an excursion parameter led to extensive turbulent dissipation and mixing. Although the present simulations do not directly simulate these dissipative and turbulent processes, the model may be accounting for them through elevated numerical dissipation or simply via bottom friction due to the quadratic drag law. This is highlighted by the fact that the BC radiation terms are always negative for small values of ϵ_1 and ϵ_2. In these regimes the baroclinic energy is being lost to (modeled) dissipation and mixing.

c. Comparison to linear theory

A number of theoretical estimates of tidal energy conversion have been presented in previous studies (Bell 1975; Llewellyn Smith and Young 2002; Balmforth et al. 2002; St. Laurent et al. 2003; Balmforth and Peacock 2009). Using linear theory, Bell (1975) examined the tidal conversion by two-dimensional topography in the limits of $\epsilon_1 \ll 1$ and $\delta \ll 1$. Con-

sidering an ocean of constant N and an isolated ridge represented by the Witch of Agnesi profile,

$$h(x) = h_0 \left(1 + \frac{x^2}{b^2}\right)^{-1} , \tag{49}$$

Bell's estimate of the tidal conversion, in units of W, is given by

$$C_{Bell} = \frac{\pi}{8}\rho_0 U_0^2 h_0^2 L \frac{N\sqrt{\omega^2 - f^2}}{\omega} , \tag{50}$$

where L is the length of the topography. Note that C_{Bell} is independent of the width b of the ridge. Llewellyn Smith and Young (2002) extended Bell's result to an ocean of finite depth but assumed $\epsilon_1 \ll 1$ and $\epsilon_2 \ll 1$. For the same ridge, they estimated the tidal conversion, in units of W, as

$$C_{LSY} = \frac{\pi}{8}\rho_0 U_0^2 h_0^2 L \frac{\sqrt{(N^2 - \omega^2)(\omega^2 - f^2)}}{\omega} \frac{c^2 e^{-c}}{(1 - e^{-c})^2} , \tag{51}$$

where $c = \left(3^{3/2}\pi/4\right)(\delta/\epsilon_1)$. Balmforth et al. (2002) kept the infinite depth assumption ($\delta \ll 1$) but extended the small slope limit ($\epsilon_1 \ll 1$) to the full subcritical range ($0 \leq \epsilon_1 < 1$). As ϵ_1 increases, the conversion rate is enhanced smoothly and modestly above Bell's estimate. As $\epsilon_1 \to 1$, the enhancement is 56% for sinusoidal topography while only 14% for a Gaussian bump and roughly 6% for random topography. St. Laurent et al. (2003) further examined the tidal conversion at abrupt topography. For a knife-edge ridge ($\epsilon_1 \to \infty$), their estimate of the tidal conversion, in units of W, is given by

$$C_{StL} = \frac{1}{2\pi}\rho_0 U_0^2 H^2 L \frac{\sqrt{(N^2 - \omega^2)(\omega^2 - f^2)}}{\omega} \sum_{n=1}^{\infty} n^{-1} a_n^2 , \tag{52}$$

where n is the vertical mode number, a_n are obtained by solving the matrix problem $A_{mn}a_n = c_m$. The formation of matrix A_{mn} and vector c_m are given by equations (17)-(20) in St. Laurent et al. (2003).

We compare our simulated tidal energy conversion to the theoretical estimates (50)-(52). The Davidson Seamount is a relatively isolated, ridge-like feature ($\epsilon_1 = 2$) with its peak $\sim$1500 m below the sea surface. It has a length scale of roughly $L = 40$ km and an amplitude of $h_0 = 1500$ m ($\delta = 0.5$). The mean barotropic tidal current over this region is approximately 3 cm s^{-1}. At the depths of the Davidson Seamount the ocean stratification is close to linear, which results in a nearly constant $N = 1 \times 10^{-3}$ s^{-1}. Using these numbers and constant values of $\rho_0 = 1000$ kg m^{-3}, $\omega = \omega_{M_2} = 1.4053 \times 10^{-4}$ rad s^{-1}, $f = 8.7 \times 10^{-5}$ rad s^{-1}, we obtain Bell's estimate from equation (50) as $C_{Bell} = 24.98$ MW, and Llewellyn Smith and Young's estimate from equation (51) as $C_{LSY} = 22.92$ MW. The estimate of St. Laurent et al. is obtained from equation (52) as $C_{StL} = 37.02$ MW for 1000 vertical modes. These theoretical results and our model estimate (28.24 MW) are of the same order of magnitude. The first two theoretical estimates are derived in the limit of $\epsilon_1 \ll 1$ and therefore underestimate the supercritical conversion by the Davidson Seamount based on the studies of Balmforth et al. (2002) and St. Laurent et al. (2003). The third theoretical estimate is derived in the limit of $\epsilon_1 \to \infty$, and thus may overestimate the conversion by the Davidson Seamount.

We do not compare the model and theoretical estimates for the entire domain because $\delta \to 1$ in the shelf-slope and the stratification of the upper ocean is strongly nonlinear (i.e. N increases by an order of magnitude from a depth of 1500 m to a depth of 25 m). With such variable N, finite ϵ_1 and $\delta \to 1$, it is difficult to estimate the energy conversion using equations (50)-(52) (Garrett and Kunze 2007).

6. Summary and discussion

We have performed a detailed energy analysis of the barotropic and baroclinic M_2 tides in the Monterey Bay area. A theoretical framework for analyzing internal tide energetics is derived based on the complete form of the barotropic and baroclinic energy equations. These equations provide a more accurate and detailed energy analysis because they include the full nonlinear and nonhydrostatic energy flux contributions as well as an improved evaluation of the available potential energy. Three-dimensional, high-resolution simulations of the barotropic and baroclinic tides in the Monterey Bay area are conducted using the hydrodynamic SUNTANS model. Based on the theoretical approach, model results are analyzed to address the question of how the barotropic tidal energy is partitioned between local barotropic dissipation and local generation of baroclinic energy, and then how much of this generated baroclinic energy is lost locally versus how much is radiated away for open-ocean mixing. Subdomain (a), a 200 km $\times$ 230 km domain, is used to represent the Monterey Bay area because it includes all typical topographic features in this region. Of the 152 MW energy lost from the barotropic tide, approximately 133 MW (88%) is converted into baroclinic energy through internal tide generation, and 42% (56 MW) of this baroclinic energy radiates away for open-ocean mixing (Figure 14). The tidal energy partitioning depends greatly on the topographic features. The Davidson Seamount and the Northern shelf-break region are most efficient at baroclinic energy generation ($\sim$ 94%) and radiation ($>$ 70%). The Sur Platform region converts a large portion ($\sim$ 88%) and radiates roughly half of the barotropic energy as baroclinic energy. The MSC acts as an energy sink because it does not radiate energy but instead absorbs the baroclinic energy from the Sur Platform region.

The energy flux contributions from nonlinear and nonhydrostatic effects are also examined. The small advection and nonhydrostatic contributions imply that the internal tides in the Monterey Bay area are predominantly linear and hydrostatic.

We also investigate the character of internal tide generation by examining the energy distribution as a function of two nondimensional parameters, namely the steepness parameter ($\epsilon_1 = \gamma/s$) and the excursion parameter ($\epsilon_2 = U_0 k_b/\omega$). The generation mainly occurs in the regions satisfying $\epsilon_1 < 5$ and $\epsilon_2 < 0.06$, indicating that baroclinic tides generated in the Monterey Bay area are mainly linear and in the form of internal tidal beams. The results highlight how description of the conversion process with simple nondimensional parameters produces results that are consistent with theory, in that internal wave energy generation peaks at critical topography ($\epsilon_1 \sim 1$). The results also indicate that conversion peaks for a particular excursion parameter ($\epsilon_2 \sim 0.005$ for this case). This implies that it may be possible to parameterize conversion of barotropic to baroclinic energy in barotropic models with knowledge of ϵ_1 and ϵ_2. For example, a parameterization of internal wave generation based on the steepness parameter has been widely used in global barotropic tidal models (Jayne and St. Laurent 2001; St. Laurent et al. 2002) and ocean general circulation models (Simmons et al. 2004; Jayne 2009).

To demonstrate that parameterizations of internal wave energy generation produce results that are valid even in complex domains with complex topography and tidal currents, we compare the model estimate of the barotropic-to-baroclinic conversion with three theoretical results. The Davidson Seamount ($\epsilon_1 = 2$) is chosen as a comparison region because it mostly satisfies the assumptions under which the theoretical estimates were derived. The theoretical and model estimates are of the same order of magnitude. The model estimate is slightly

larger than the first two theoretical estimates that were derived in the limit of $\epsilon_1 \ll 1$ (Bell 1975; Llewellyn Smith and Young 2002), while it is smaller than the third theoretical estimate that was derived in the limit of $\epsilon_1 \to \infty$ (St. Laurent et al. 2003). Moreover, the energy budget for the Davidson Seamount is quite similar to that for the Hawaiian Islands in a previous model study by Carter et al. (2008). They showed that the Hawaiian Ridge converts 85% of the barotropic energy into baroclinic energy, and then radiates 74% of this baroclinic energy into the open ocean. In our study, the Davidson Seamount converts 95% of the barotropic energy into baroclinic energy, and then radiates 81% of this baroclinic energy away for open-ocean mixing.

This work outlines a systematic approach to analyze internal tide energetics and estimate tidal energy budget regionally and globally. The results draw a picture of how the M_2 tidal energy is distributed in the Monterey Bay region. However, the simulation is limited to only one stratification taken in late summer of 2006. The stratification is specified as horizontally uniform throughout the domain as an initial condition. Earlier internal tide observations (Petruncio et al. 1998) and simulations (Rosenfeld et al. 2009; Wang et al. 2009) indicate that the internal tides are sensitive to stratification. The Monterey Bay area is exposed to the large-scale California Current System and meso-scale eddies and upwelling. The seasonally varying dynamics may affect the stratification and thus the generation and propagation of internal tides in this area. Therefore, it may be necessary to consider seasonal effects of stratification and to include mesoscale effects by coupling with a larger-scale regional model such as ROMS (Haidvogel et al. 2000; Shchepetkin and McWilliams 2005).

Acknowledgments.

The authors gratefully acknowledge the support of ONR Grant N00014-05-1-0294 (Scientific officers: Drs. C. Linwood Vincent, Terri Paluszkiewicz, and Scott Harper). We would like to thank Samantha Brody, Drs. Jody Klymak, Robert Pinkel, James Girton, and Eric Kunze for kindly providing the field data. The helpful discussions with Drs. Robert Street, Stephen Monismith, Leif Thomas, and Rocky Geyer are greatly appreciated. We also thank Dr. Steven Jachec for useful help with simulation setup. Comments and suggestions from four anonymous reviewers greatly helped to improve the manuscript.

APPENDIX

Inferred vs. Modeled Dissipation

A set of M_2-forced numerical simulations are carried out to examine the sensitivity of model results to the dissipation parameters. The reference simulation (simulation 0) is that discussed in Section 4, which employs the constant eddy viscosities ($\nu_H = 1$ m^{2}s^{-1} and $\nu_V = 5\times10^{-3}$ m^{2}s^{-1}) and a constant bottom drag coefficient ($C_d = 0.0025$). In simulations 1-6, the values of ν_H or ν_V or C_d is changed by one order of magnitude. For each simulation, we calculate the domain-integrated, period-averaged baroclinic energy terms for subdomain (a) in Figure 6. They are the barotropic-to-baroclinic conversion (37), the baroclinic radiation (38), the inferred baroclinic dissipation (40) and the directly computed baroclinic dissipation ($\sum \left\langle \overline{\epsilon'} + D' \right\rangle \Delta A$). Detailed comparisons are listed in Table 4.

If we consider the effect of numerical error, the period-averaged baroclinic energy equation (25) gives the following balance relation

$$\begin{aligned} & \text{Conversion} - \text{Radiation} \\ = \; & \text{Inferred Dissipation} + \text{Error}\,, \\ = \; & \text{Modeled Dissipation} + \text{Numerical Dissipation} + \text{Error}\,, \end{aligned} \tag{A1}$$

where "Numerical Dissipation" results primarily from the numerical diffusion associated with scalar and momentum advection and "Error" arises from the assumption of periodicity. For a periodic system, "Error" should tend to zero. This is what we saw in the last six M_2

tidal cycles of the simulations. Table 4 shows that changing the dissipation parameters by one order of magnitude has a minor effect on Conversion, Radiation and hence the Inferred Dissipation. However, the directly computed dissipation (or Modeled Dissipation) depends greatly on the dissipation parameters. For example, increasing/decreasing ν_V by one order of magnitude roughly doubles/halves the modeled dissipation. Similarly, increasing/decreasing C_d by one order of magnitude causes a 74% increase/9% decrease in modeledl dissipation. Interestingly, an increase/decrease of ν_H results in a decrease/increase in modeled dissipation. This may imply that increasing ν_H smears out gradients so that the impact is to reduce $\nu_H \nabla_H \mathbf{u}' \cdot \nabla_H \mathbf{u}'$ since $\nabla_H \mathbf{u}'$ decreases by more than ν_H increases. Overall, this set of sensitivity tests show that the Inferred Dissipation is nearly a constant, while the Modeled Dissipation is a strong function of the dissipation parameters. Based on the balance relation (A1), the Numerical Dissipation also depends greatly on the dissipation parameters.

In the numerical simulations, the values of the diffusion parameters are set by the stability requirements of numerical differencing and are not necessarily the realistic ocean values. Moreover, in the real ocean the eddy viscosities and bottom drag are functions of location and time, while in the simulations we only apply a constant value for each throughout the domain. Therefore, although we are able to compute the dissipation directly, it may not represent the true physical dissipation in the real ocean. For this reason, the inferred dissipation, which is virtually independent of the dissipation parameters, is used for the energy analysis in Section 4.

REFERENCES

Balmforth, N. J., G. R. Ierley, and W. R. Young, 2002: Tidal conversion by subcritical topography. *J. Phys. Oceanogr.*, **32**, 2900–2914.

Balmforth, N. J. and T. Peacock, 2009: Tidal conversion by supercritical topography. *J. Phys. Oceanogr.*, **39**, 1965–1974.

Bell, T. H., 1975: Topographically generated internal waves in the open ocean. *J. Geophys. Res.*, **80**, 320–327.

Blayo, E. and L. Debreu, 2005: Revisiting open boundary conditions from the point of view of characteristic variables. *Ocean Modelling*, **9**, 231–252.

Blumberg, A. F. and G. L. Mellor, 1987: A description of a three-dimensional coastal ocean circulation model. *Three-Dimensional Coastal Ocean Models, N. Heaps (Eds.), Amer. Geophys. Union*, 1–16.

Buijsman, M. C., Y. Kanarska, and J. C. McWilliams, 2010: On the generation and evolution of nonlinear internal waves in the South China Sea. *J. Geophys. Res.*, **115**, C02 012, doi:10.1029/2009JC005 275.

Carter, G. S., 2010: Barotropic and baroclinic M2 tides in the Monterey Bay region. *J. Phys. Oceanogr.*, **40**, 1766–1783.

Carter, G. S. and M. C. Gregg, 2002: Intense, variable mixing near the head of Monterey Submarine Canyon. *J. Phys. Oceanogr.*, **32**, 3145–3165.

Carter, G. S., et al., 2008: Energetics of M2 barotropic-to-baroclinic tidal conversion at the Hawaiian Islands. *J. Phys. Oceanogr.*, **38**, 2205–2223.

Cummins, P. F. and L. Oey, 1997: Simulation of barotropic and baroclinic tides off northern British Columbia. *J. Phys. Oceanogr.*, **27**, 762–781.

Egbert, G. D. and S. Y. Erofeeva, 2002: Efficient inverse modeling of barotropic ocean tides. *J. Atmos. Oceanic Technol.*, **19**, 183–204.

Egbert, G. D. and R. D. Ray, 2000: Significant dissipation of tidal energy in the deep ocean inferred from satellite altimeter data. *Nature*, **405**, 775–778.

Egbert, G. D. and R. D. Ray, 2001: Estimates of M2 tidal energy dissipation from TOPEX/Poseidon altimeter data. *J. Geophys. Res.*, **106(C10)**, 22 475–22 502.

Fringer, O. B., M. Gerritsen, and R. L. Street, 2006: An unstructured-grid, finite-volume, nonhydrostatic, parallel coastal ocean simulator. *Ocean Modelling*, **14**, 139–173, doi:10.1016/j.ocemod.2006.03.006.

Garrett, C. and E. Kunze, 2007: Internal tide generation in the deep ocean. *Annu. Rev. Fluid Mech.*, **39**, 57–87.

Gill, A. E., 1982: *Atmosphere-Ocean Dynamics*. Academic Press.

Haidvogel, D. B., H. G. Arango, K. Hedstrom, A. Beckmann, P. Malanotte-Rizzoli, and A. F. Shchepetkin, 2000: Model evaluation experiments in the North Atlantic Basin: Simulations in nonlinear terrain-following coordinates. *Dyn. Atmos. Oceans*, **32**, 239–281.

Hall, R. A. and G. S. Carter, 2011: Internal tides in Monterey Submarine Canyon. *J. Phys. Oceanogr.*, **41**, 186–204.

Jachec, S. M., 2007: *Understanding the evolution and energetics of internal tides within Monterey Bay via numerical simulations*. Ph.D. Dissertation, Stanford University.

Jachec, S. M., O. B. Fringer, M. G. Gerritsen, and R. L. Street, 2006: Numerical simulation of internal tides and the resulting energetics within Monterey Bay and the surrounding area. *Geophys. Res. Lett.*, **33**, L12 605, doi:10.1029/2006GL026 314.

Jayne, S. R., 2009: The impact of abyssal mixing parameterizations in an ocean general circulation model. *J. Phys. Oceanogr.*, **39**, 1756–1775.

Jayne, S. R. and L. C. St. Laurent, 2001: Parameterizing tidal dissipation over rough topography. *Geophys. Res. Lett.*, **28**, 811–814.

Kang, D., 2010: *Energetics and dynamics of internal tides in Monterey Bay using numerical simulations*. Ph.D. Dissertation, Stanford University.

Kang, D. and O. B. Fringer, 2010: On the calculation of available potential energy in internal wave fields. *J. Phys. Oceanogr.*, **40**, 2539–2545.

Khatiwala, S., 2003: Generation of internal tides in an ocean of finite depth: analytical and numerical calculations. *Deep-Sea Res. I*, **50**, 3–21.

Kunze, E., L. K. Rosenfeld, G. S. Carter, and M. C. Gregg, 2002: Internal waves in Monterey Submarine Canyon. *J. Phys. Oceanogr.*, **32**, 1890–1913.

Kurapov, A. L., J. S. Allen, and G. D. Egbert, 2010: Combined effects of wind-driven upwelling and internal tide on the continental shelf. *J. Phys. Oceanogr.*, **40**, 737–756.

Lamb, K. G., 2007: Energy and pseudoenergy flux in the internal wave field generated by tidal flow over topography. *Cont. Shelf Res.*, **27**, 1208–232.

Lamb, K. G. and V. T. Nguyen, 2009: Calculating energy flux in internal solitary waves with an application to reflectance. *J. Phys. Oceanogr.*, **39**, 559–580.

Legg, S. and K. M. H. Huijts, 2006: Preliminary simulations of internal waves and mixing generated by finite amplitude tidal flow over isolated topography. *Deep-Sea Res. II*, **53**, 140–156.

Legg, S. and J. Klymak, 2008: Internal hydraulic jumps and overturning generated by tidal flow over a tall steep ridge. *J. Phys. Oceanogr.*, **38**, 1949–1964.

Llewellyn Smith, S. G. and W. R. Young, 2002: Conversion of barotropic tide. *J. Phys. Oceanogr.*, **32**, 1554–1566.

MacCready, P., N. S. Banas, B. M. Hickey, E. P. Dever, and Y. Liu, 2009: A model study of tide- and wind-induced mixing in the Columbia River Estuary and plume. *Contin. Shelf Res.*, **29**, 278–291.

Manders, A. M. M., L. R. M. Maas, and T. Gerkema, 2004: Observations of internal tides in the Mozambique Channel. *J. Geophys. Res.*, **109**, C12 034, doi:10.1029/2003JC002 187.

Merrifield, M. A., P. Holloway, and T. Johnston, 2001: The generation of internal tides at the Hawaiian Ridge. *Geophys. Res. Lett.*, **28**, 559–562.

Merrifield, M. A. and P. E. Holloway, 2002: Model estimates of M2 internal tide energetics at the Hawaiian Ridge. *J. Geophys. Res.*, **107**, 3179, doi:10.1029/2001JC000 996.

Millero, F. J., C.-T. Chen, A. Bradshaw, and K. Schleicher, 1980: A new high pressure equation of state for seawater. *Deep-Sea Res. A*, **27**, 255–264.

Millero, F. J. and A. Poisson, 1981: International one-atmosphere equation of state of seawater. *Deep-Sea Res. A*, **28**, 625–629.

Munk, W. and C. Wunsch, 1998: Abyssal recipes II: Energetics of tidal and wind mixing. *Deep-Sea Res.*, **45**, 1977–2010.

Niwa, Y. and T. Hibiya, 2004: Three-dimensional numerical simulation of M2 internal tides in the East China Sea. *J. Geophys. Res.*, **109**, C04 027, doi:10.1029/2003JC001 923.

Pawlowicz, R., B. Beardsley, and S. Lentz, 2002: Classical tidal harmonic analysis including error estimates in MATLAB using T-TIDE. *Computers & Geosciences*, **28**, 929–937.

Petruncio, E. T., L. K. Rosenfeld, and J. D. Paduan, 1998: Observations of the internal tide in Monterey Canyon. *J. Phys. Oceanogr.*, **28**, 1873–1903.

Rosenfeld, L. K., I. Shulman, M. Cook, J. B. Paduan, and L. Shulman, 2009: Methodology for a regional tidal model evaluation, with application to central California. *Deep-Sea Res. II*, **56**, 199–218.

Scotti, A., R. Beardsley, and B. Butman, 2006: On the interpretation of energy and energy fluxes of nonlinear internal waves: an example from Massachusetts Bay. *J. Fluid Mech.*, **561**, 103–112.

Shchepetkin, A. and J. C. McWilliams, 2005: The Regional Oceanic Modeling System: A split-explicit, free-surface, topography-following-coordinate ocean model. *Ocean Modelling*, **9**, 347–404.

Simmons, H. L., S. R. Jayne, L. C. St. Laurent, and A. J. Weaver, 2004: Tidally driven mixing in a numerical model of the ocean general circulation. *Ocean Modelling*, **6**, 245–263, doi:10.1016/S1463–5003(03)00 011–8.

St. Laurent, L. and C. Garrett, 2002: The role of internal tides in mixing the deep ocean. *J. Phys. Oceanogr.*, **32**, 2882–2899.

St. Laurent, L., S. Stringer, C. Garrett, and D. Perrault-Joncas, 2003: The generation of internal tides at abrupt topography. *Deep-Sea Res. I*, **50**, 987–1003.

St. Laurent, L. C., H. L. Simmons, and S. R. Jayne, 2002: Estimating tidally driven mixing in the deep ocean. *Geophys. Res. Lett.*, **29**, doi:10.1029/2002GL015 633.

Terker, S. R., J. B. Girton, and E. Kunze, 2011: Observations of the internal tide on the California continental margin near Monterey Bay. *Cont. Shelf Res.*, submitted.

Venayagamoorthy, S. K. and O. B. Fringer, 2007: On the formation and propagation of nonlinear internal boluses across a shelf break. *J. Fluid Mech.*, **577**, 137–159, doi:10.1017/S0022112007004 624.

Vitousek, S. and O. B. Fringer, 2011: Physical vs. numerical dispersion in nonhydrostatic ocean modeling. *Ocean Modelling*, **40**, 72–86, doi:10.1016/j.ocemod.2011.07.002.

Vlasenko, V., N. Stashchuk, and K. Hutter, 2005: *Baroclinic Tides: Theoretical Modeling and Observational Evidence*. Cambridge University Press.

Wang, X., Y. Chao, C. Dong, J. Farrara, Z. Li, J. C. McWilliams, P. J. D., and L. K. Rosenfeld, 2009: Modeling tides in Monterey Bay, California. *Deep-Sea Res. II*, **56**, 219–231.

Zhang, Z., 2010: *Numerical simulation of nonlinear internal waves in the South China Sea*. Ph.D. Dissertation, Stanford University.

Zhang, Z., O. B. Fringer, and S. R. Ramp, 2011: Three-dimensional, nonhydrostatic numerical simulation of nonlinear internal wave generation and propagation in the South China Sea. *J. Geophys. Res.*, **116**, C05 022, doi:10.1029/2010JC006 424.

Zilberman, N. V., J. M. Becker, M. A. Merrifield, and G. S. Carter, 2009: Model estimates of M2 internal tide generation over Mid-Atlantic Ridge topography. *J. Phys. Oceanogr.*, **39**, 2635–2651.

List of Tables

TABLE 1. M_2 tidal energy budget for the five subdomains indicated in Figure 6. The energy in estimated in MW.

Domains	(a)	(b)	(c)	(d)	(e)
BT Input	151.95	31.04	8.30	44.80	29.82
	(100%)	(100%)	(100%)	(100%)	(100%)
BT-BC Conversion	133.39	29.17	5.85	39.20	28.24
	(88%)	(94%)	(70.5%)	(87.5%)	(94.7%)
BC Radiation	56.20	22.05	-3.64	24.02	22.91
	(37%)	(71%)	(-44%)	(53.6%)	(76.8%)
BT Dissipation	-18.56	-1.87	-2.45	-5.60	-1.58
	(12%)	(6%)	(29.5%)	(12.5%)	(5.3%)
BC Dissipation	-77.19	-7.12	-9.49	-18.42	-5.33
	(51%)	(23%)	(114.5%)	(33.9%)	(17.9%)
Total Dissipation	-95.75	-8.99	-11.94	-20.78	-6.91
	(63%)	(29%)	(144%)	(46.4%)	(23.2%)

TABLE 2. Contributions of different energy fluxes to the total baroclinic energy flux divergence for subdomain (a). The contributions are estimated in percentages.

$\sum_{(a)} \left(\nabla_H \cdot \overline{\mathbf{F}'} \right)$	100%
KE Advection	-0.54%
APE Advection	0.18%
Hydrostatic Work	100.87%
Nonhydrostatic Work	-0.51%
Diffusion	0.002%

TABLE 3. Key physical parameters governing internal tide generation and propagation.

Parameters	Descriptions
ω	tidal frequency
f	Coriolis frequency
N	buoyancy frequency
U_0	amplitude of the barotropic tidal current
k	horizontal wavenumber of the internal tide
m	vertical wavenumber of the internal tide
c	phase speed of the internal tide ($c = \omega/k$)
k_b	horizontal wavenumber of the topography
h	height of the topography
h_0	amplitude of the topography
d	water depth
H	total water depth

TABLE 4. Sensitivity test of various simulation parameters.

Sim.	ν_H	ν_V	C_d	Grid	Bathy.	Conversion	BC Radiation	BC Diss. (direct)	BC Diss. (inferred)
	$[m^2s^{-1}]$					[MW] (relative change to Simulation 0)			
0	1	5×10^{-3}	2.5×10^{-3}	Fine	Fine	133.39	56.20	23.36	77.19
1	0.1	5×10^{-3}	2.5×10^{-3}	Fine	Fine	133.90 (+0.38%)	56.40 (+0.36%)	24.43 (+4.59%)	77.50 (+0.40%)
2	10	5×10^{-3}	2.5×10^{-3}	Fine	Fine	132.39 (-0.75%)	54.71 (-2.65%)	21.00 (-10.09%)	77.68 (+0.63%)
3	1	5×10^{-4}	2.5×10^{-3}	Fine	Fine	133.19 (-0.15%)	56.48 (+0.50%)	11.06 (-52.64%)	76.71 (-0.62%)
4	1	5×10^{-2}	2.5×10^{-3}	Fine	Fine	133.19 (-0.15%)	54.34 (-3.31%)	54.12 (+131.68%)	78.85 (+2.15%)
5	1	5×10^{-3}	2.5×10^{-4}	Fine	Fine	133.67 (+0.21%)	56.26 (+0.10%)	21.18 (-9.32%)	77.41 (-0.62%)
6	1	5×10^{-3}	2.5×10^{-2}	Fine	Fine	132.46 (-0.70%)	56.08 (-0.21%)	40.54 (+73.54%)	76.38 (-1.05%)

List of Figures

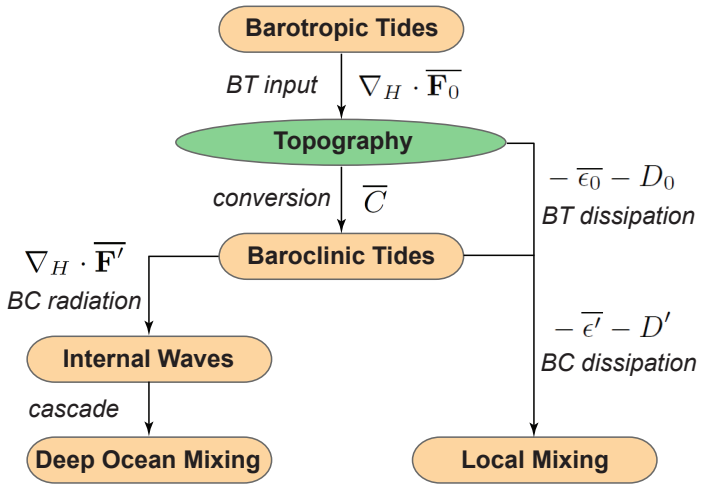

FIG. 1. Processes that transfer barotropic tidal energy to heat in the ocean. The associated energy distributions are indicated by the energy terms in the barotropic and baroclinic energy equations.

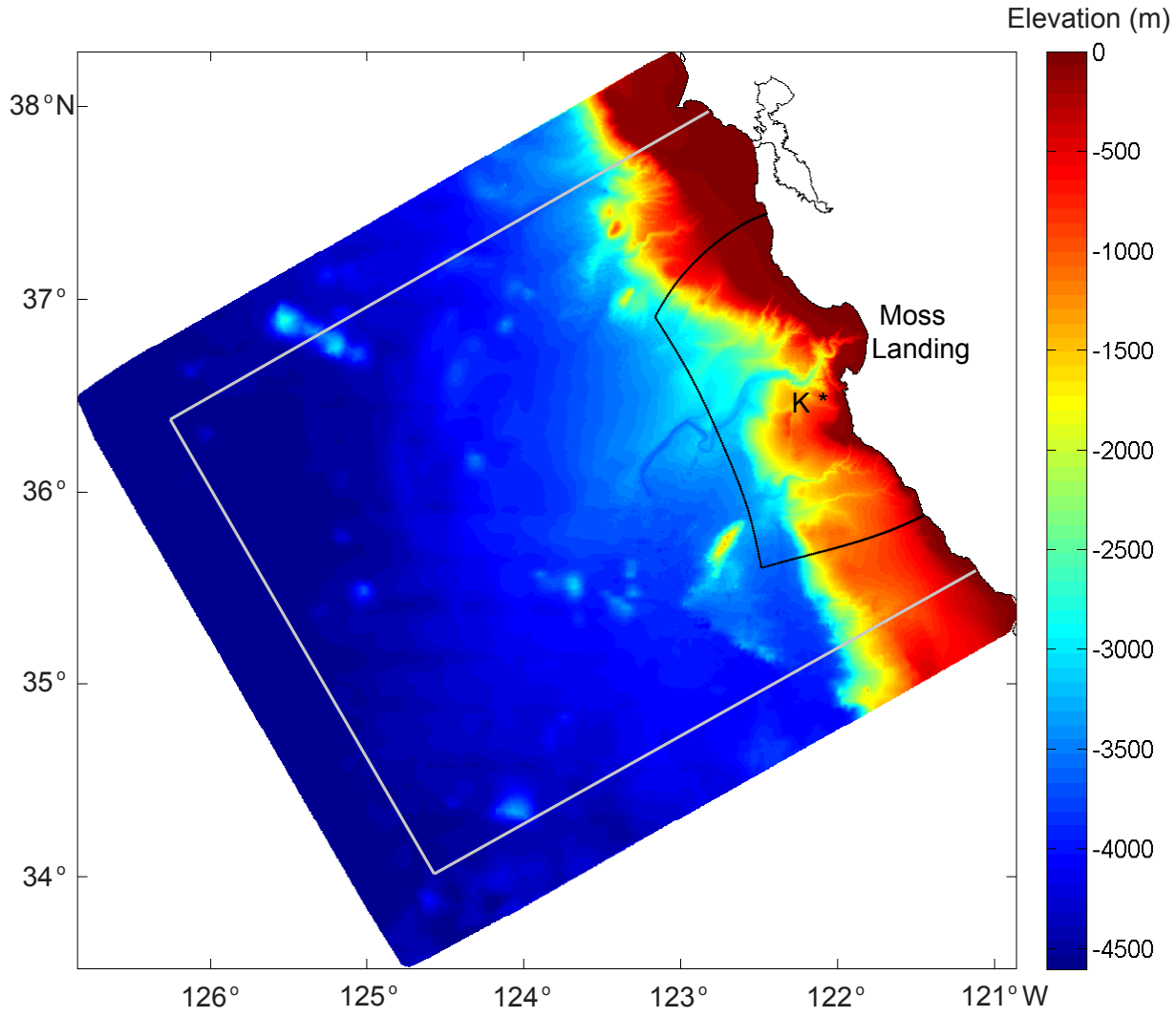

FIG. 2. Bathymetry map of Monterey Bay and the surrounding open ocean. The location of Station K is indicated by a black $*$. The domain outside the white box indicates the area affected by the sponge layers in the simulations. The domain of Jachec et al. (2006) is outlined by a solid black line.

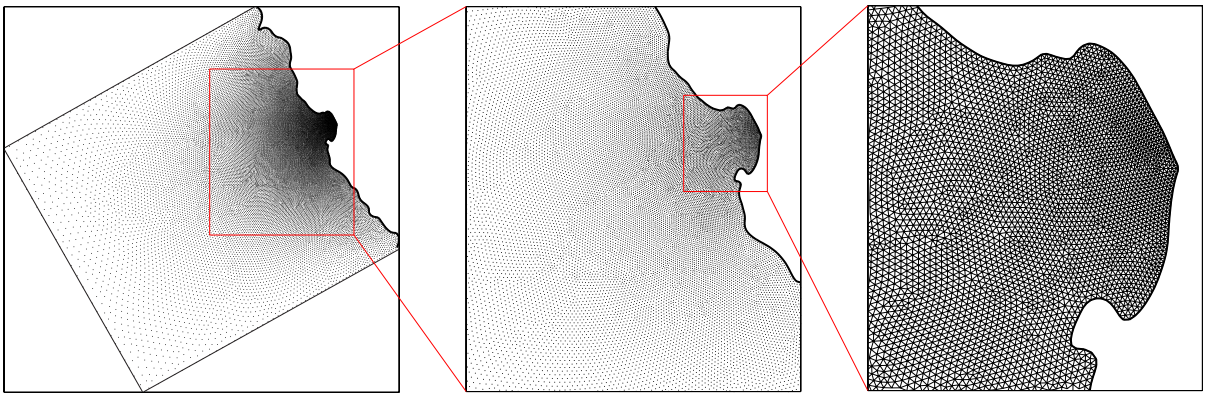

FIG. 3. The unstructured grid of the computational domain (left) and zoomed-in views for subdomain (a) indicated in Figure 6 (middle) and Monterey Bay (right). In the left two plots, only cell centers are shown for clarify, while in the right plot, cell edges are shown.

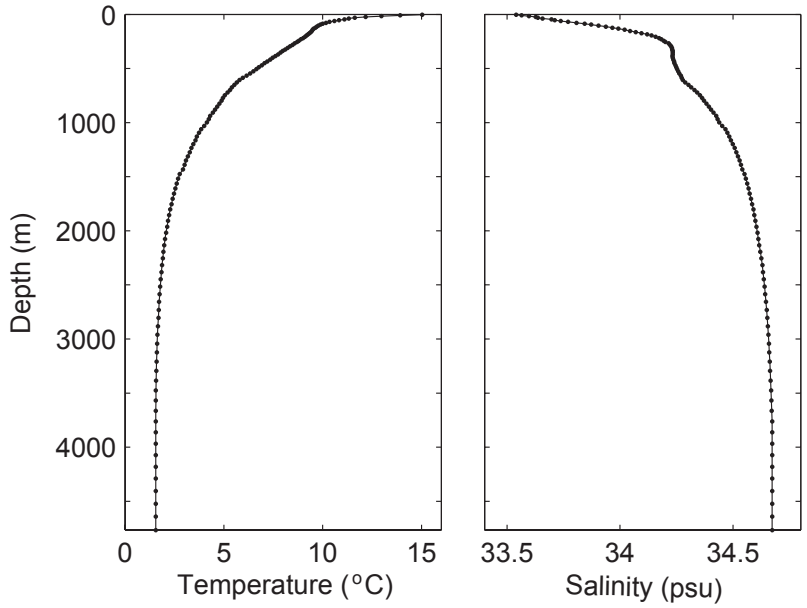

FIG. 4. Initial temperature and salinity profiles for the simulations. The black dots represent the vertical grid spacing in the simulations.

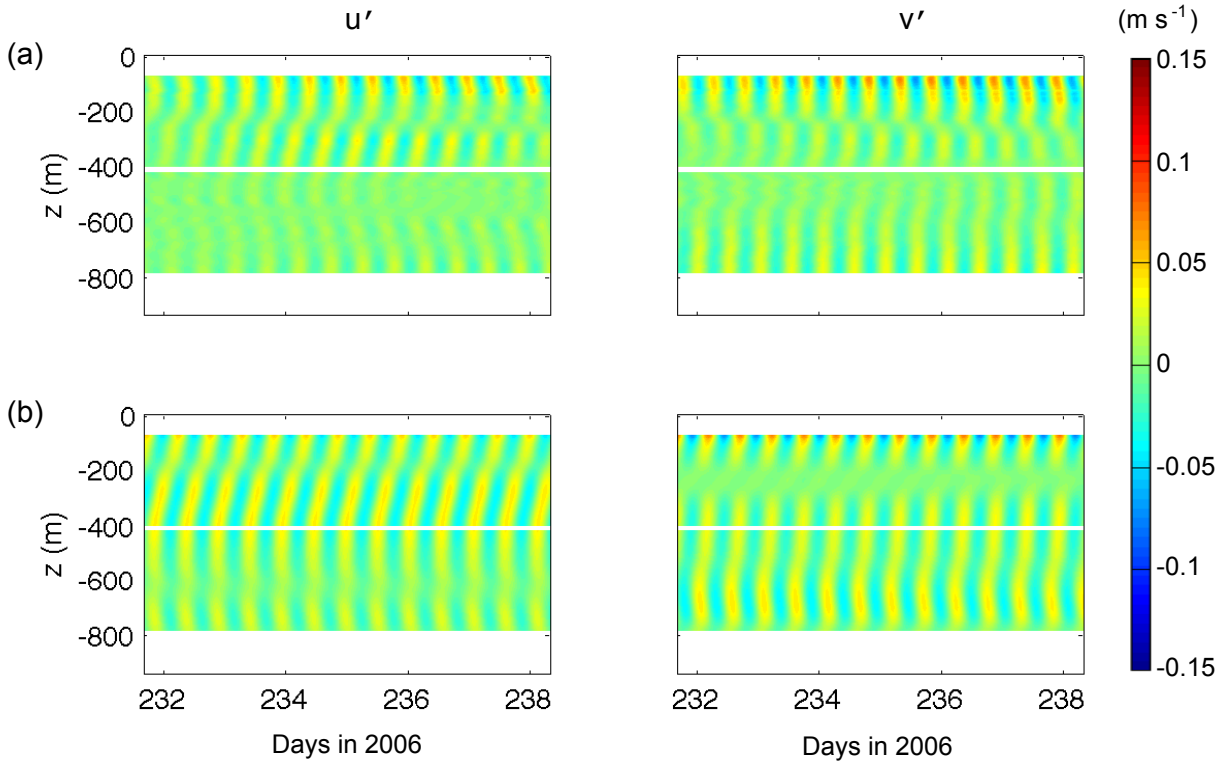

FIG. 5. Time series of the M_2 baroclinic East-West (u') and North-South (v') velocities at Station K: (a) M_2 filtered field observations; (b) SUNTANS predictions. The white areas indicate regions without observational data.

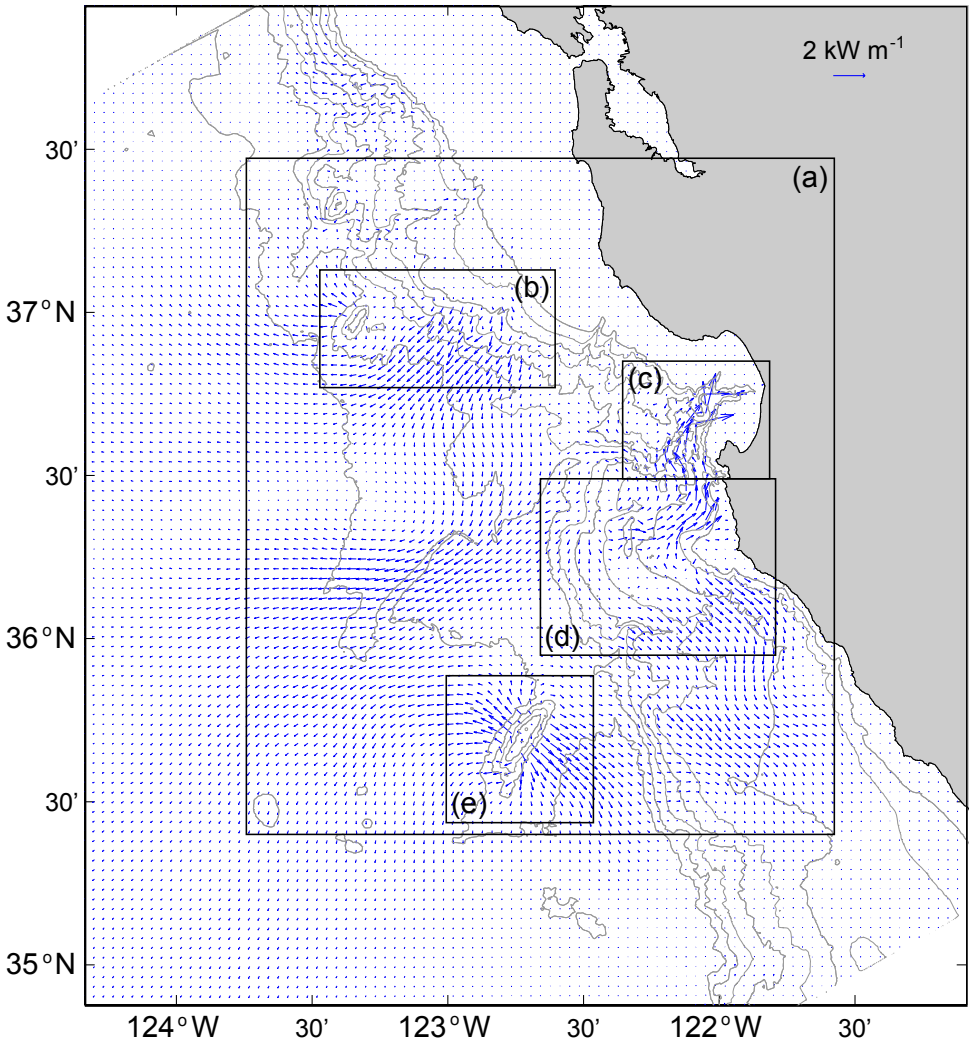

FIG. 6. Depth-integrated, period-averaged baroclinic energy flux, $\left\langle \overline{\mathbf{F}'} \right\rangle$. The five boxes (a)-(e) indicate the subdomains in which energetics are investigated in detail. Bathymetry contours are spaced at -200, -500, -1000, -1500, -2000, -2500, -3000, -3500 m.

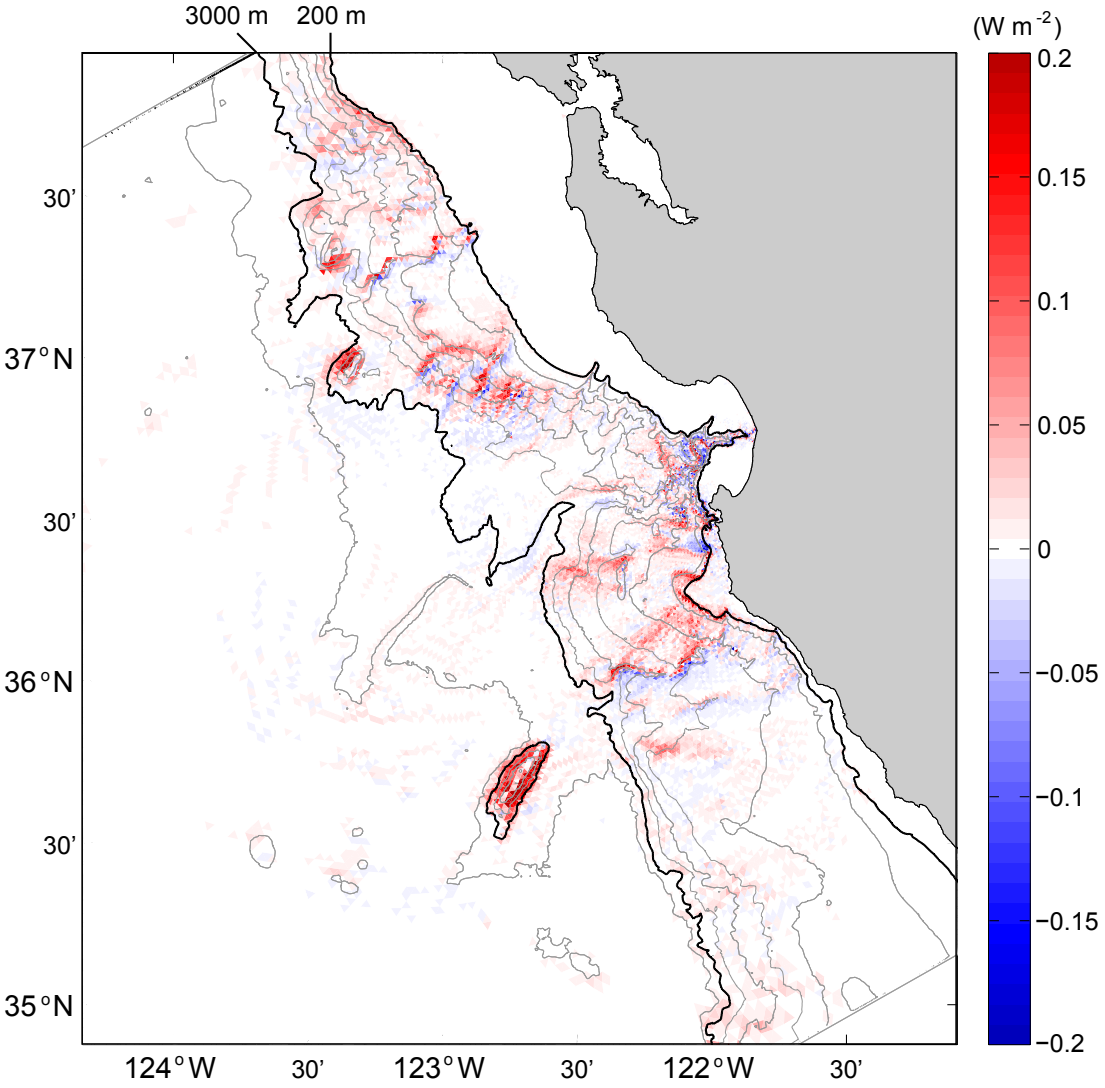

FIG. 7. Depth-integrated, period-averaged barotropic-to-baroclinic conversion rate, $\langle \overline{C} \rangle$. Bathymetry contours are spaced at -200, -500, -1000, -1500, -2000, -2500, -3000, -3500 m. Darker contours are -200 and -3000 m.

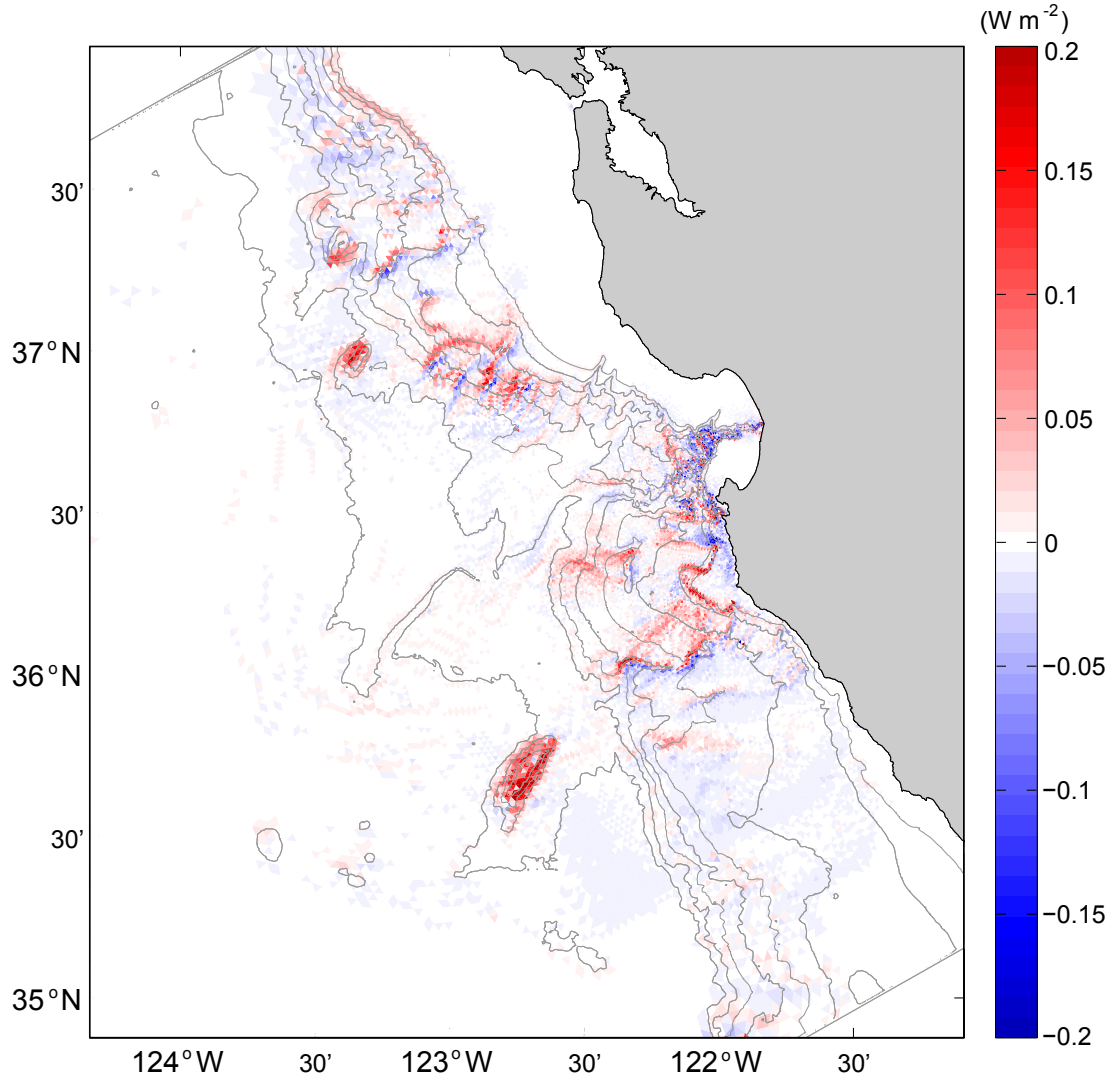

FIG. 8. Depth-integrated, period-averaged baroclinic energy flux divergence, $\nabla_H \cdot \left\langle \overline{\mathbf{F}'} \right\rangle$. Bathymetry contours are spaced at -500, -1000, -2000, -3000, -3500 m.

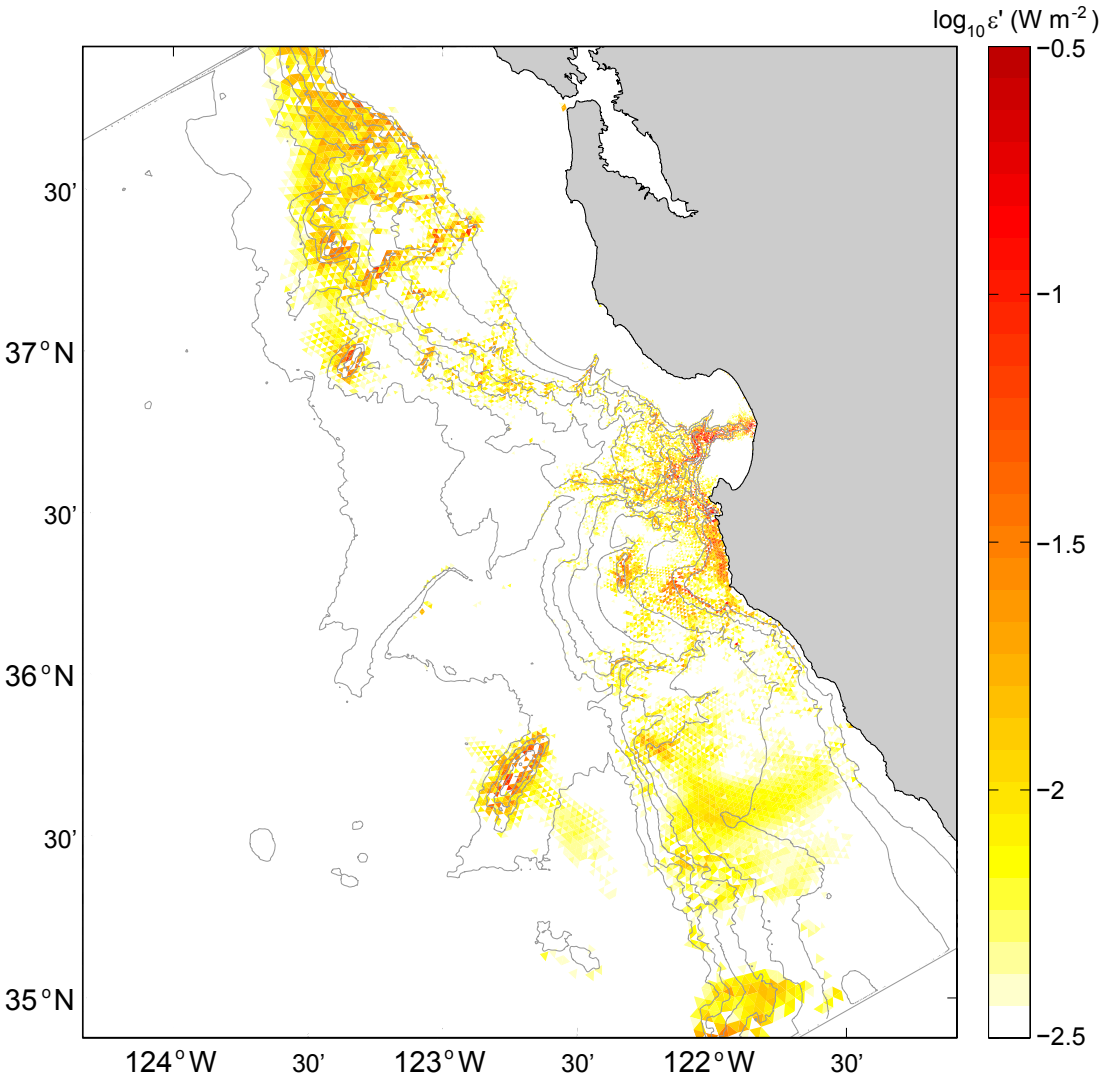

FIG. 9. Depth-integrated, period-averaged baroclinic dissipation rate, $\nabla_H \cdot \left\langle \overline{\mathbf{F}'} \right\rangle - \langle \overline{C} \rangle$. Bathymetry contours are spaced at -500, -1000, -2000, -3000, -3500 m.

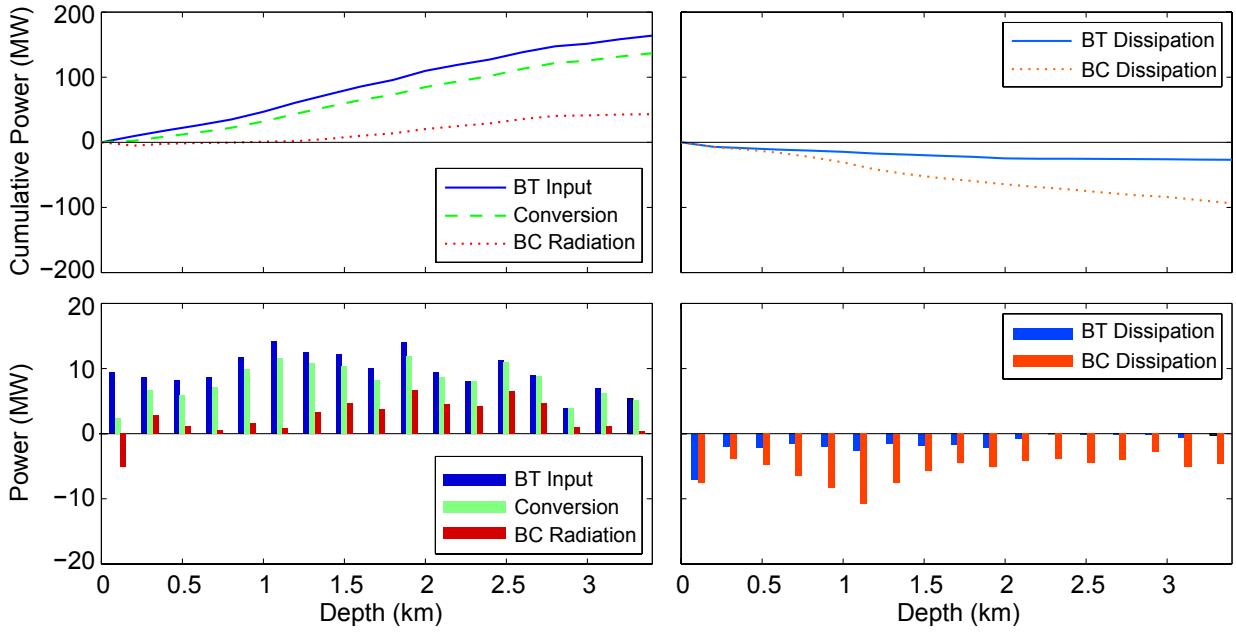

FIG. 10. Energy distribution as a function of bottom depth. Lower: energy terms (36)-(40) in 200-m isobath bounded bins; Upper: cumulative sum of the lower.

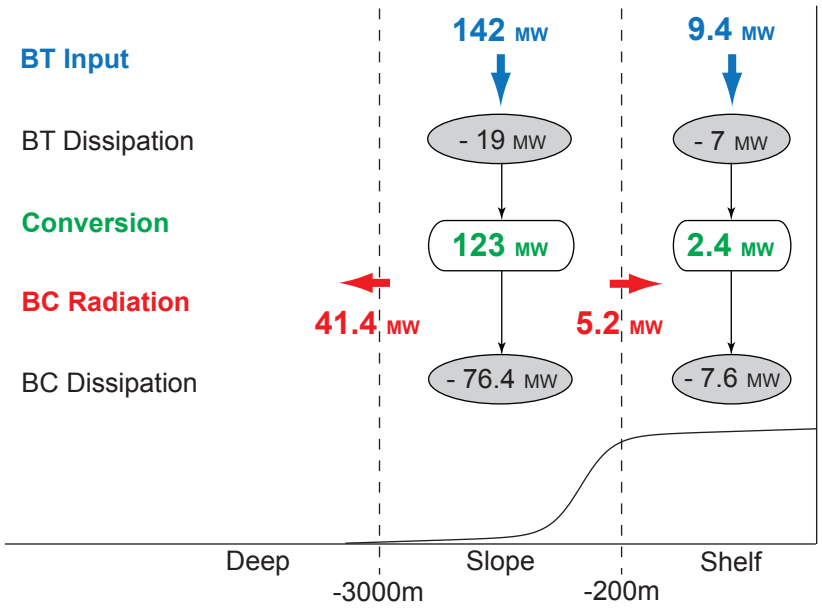

FIG. 11. Schematic of the M_2 tidal energy budget for the two subdomains bounded by the 0-m, 200-m and 3000-m isobaths.

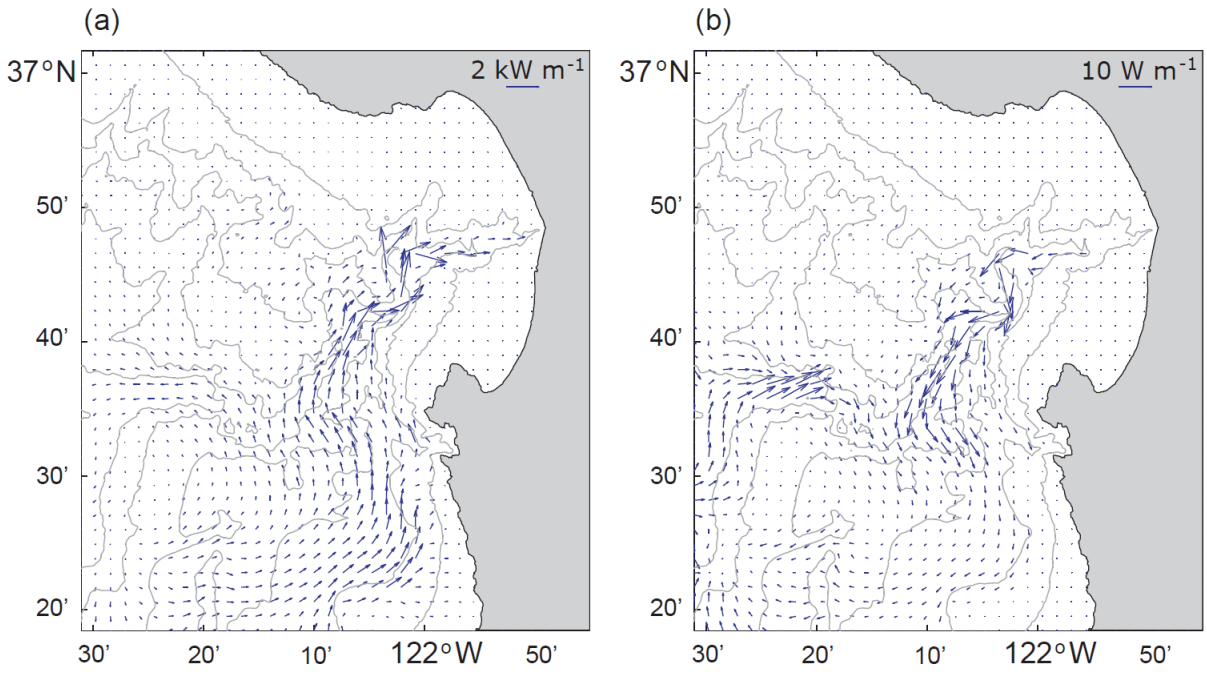

FIG. 12. Baroclinic energy flux contributions from (a) hydrostatic, and (b) nonhydrostatic pressure work in the Monterey Submarine Cayon region. Bathymetry contours are spaced at -100, -500, -1000, -1500, -2000 m.

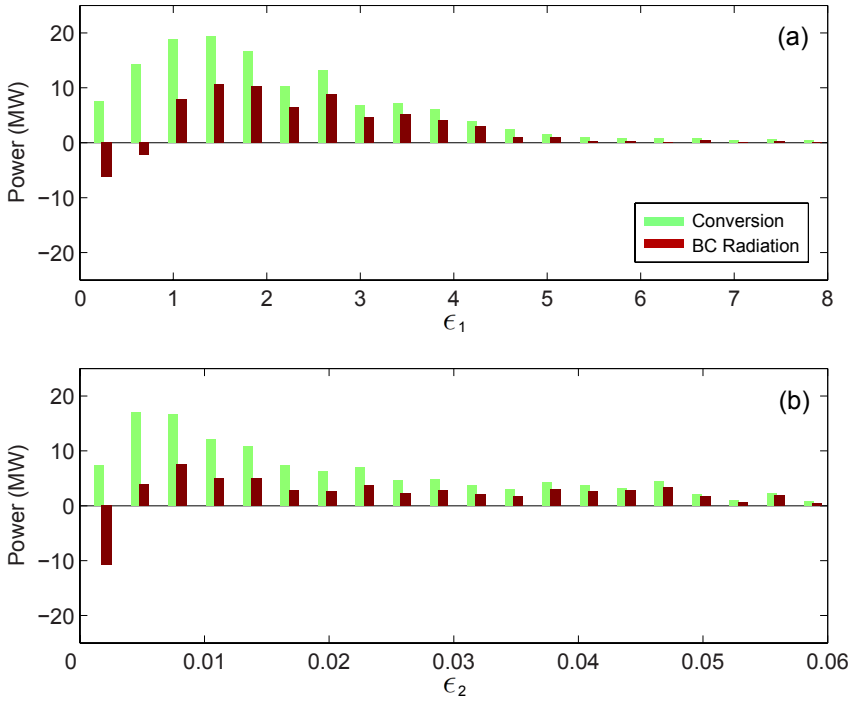

FIG. 13. Distribution of the conversion and BC radiation as a function of (a) $\epsilon_1 = \gamma/s$, and (b) $\epsilon_2 = U_0 k_b/\omega$ for subdomain (a) in Figure 6.

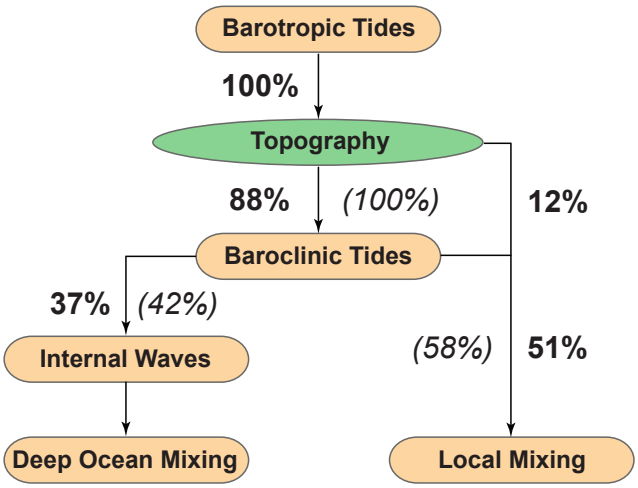

FIG. 14. Schematic of the M_2 tidal energy budget in percentages for subdomain (a) in Figure 6. The bold percentages are relative to the total input barotropic energy, and the thin italic percentages are relative to the generated baroclinic energy.